Validation of Combustion Models Using Sustainable Aviation Fuels

Master Thesis

by

Måns Larsen & David Attoff

LUND
UNIVERSITY

Department of Energy Sciences
Lund University
Sweden
19th June 2024

Supervisors: **Arvid Åkerblom**, **Professor Christer Fureby**, **Bernhard Gustafsson**
Examiner: **Professor Xue-Song Bai**

This degree project for the degree of Master of Science in Engineering has been conducted at the Department of Energy Sciences, Faculty of Engineering, Lund University.

Supervisors at the Department of Energy Sciences was Professor Christer Fureby and Arvid Åkerblom.

Supervisor at GKN Aerospace Engine Systems was Bernhard Gustafsson.

Examiner at Lund University was Professor Xue-Song Bai.

The project was carried out in cooperation with GKN Aerospace Engine Systems in Trollhättan.

© Måns Larsen and David Attoff 2024
Department of Energy Sciences
Faculty of Engineering
Lund University

ISSN: <0282-1990>
LUTMDN/TMHP-24/5590-SE

Typeset in LaTeX
Lund 2024

Acknowledgements

We would like to express our deepest gratitude to our supervisor, Christer Fureby, and co-supervisor, Arvid Åkerblom, at the Faculty of Engineering at Lund University (LTH), as well as supervisor at GKN Aerospace Engine Systems, Bernhard Gustafsson, for their invaluable guidance during the course of this thesis. Their expertise and encouragement played a pivotal role in shaping the outcome of this work. A special thanks, also, to Arvid for spending countless hours in our office dumbing down the physics theory, and explaining his convoluted MATLAB scripts.

Furthermore, we extend our sincere appreciation to the examiner, Xue-Song Bai, for his thorough evaluation and constructive feedback, which contributed to the refinement of this thesis.

Thank You!

Abstract

The aviation industry is under increasing pressure to mitigate its environmental impact, particularly concerning greenhouse gas emissions. Traditionally, commercial aviation has relied on conventional kerosene-based fuels. Recent advancements and environmental concerns have prompted the exploration of Sustainable aviation fuels (SAF), with initiatives like the Commercial Aviation Alternative Fuel Initiative (CAAFI) at the forefront of this movement. SAFs derived from renewable resources such as biomass and waste, offer a promising solution to reduce the carbon footprint of aviation operations. To further the understanding and implementation of such fuels, several studies have been conducted. While experimental studies are important, they are time-consuming and expensive, and therefore Computational Fluid Dynamics, CFD, is utilized to simulate the combustion.

This master's thesis, conducted in collaboration with GKN Aerospace Engine Systems, aims to validate combustion models for aviation fuels using commercial CFD software. The study focuses on comparing the results of different combustion models to experimental data, particularly investigating the combustion behavior and NO_x emissions of both conventional Jet A (A2) and a specific sustainable Alcohol-To-Jet (C1) fuel from Gevo. The study is conducted in the simulation tool STAR-CCM+, initially modeling turbulence with Reynolds-Averaged Navier-Stokes (RANS) and then proceeding with Large Eddy Simulation (LES). Mesh sensitivity studies are performed in both cases, also considering turbulence sensitivity. The results are validated against the benchmark case which consists of the experiments conducted at Cambridge University by Pathania *et al*.

Key findings include the superior performance of the Eddy Dissipation Concept (EDC) and Thickened Flame Model (TFM) in combustion simulations, although the EDC model showed limited applicability in LES. Flamelet Generated Manifold (FGM) showed acceptable results in LES, for its relatively low computational cost. The small comprehensive Z79 reaction mechanism demonstrated better agreement with experimental data than the HyChem skeletal reaction mechanism. Notably, C1 fuel produced higher NO_x emissions, attributed to a higher equivalence ratio and flame temperature. The study also highlights the significant impact of thermal radiation on simulation accuracy, advocating for its inclusion despite the somewhat increased computational cost.

Sammanfattning

Flygindustrin står inför ökande tryck att minska sin miljöpåverkan, särskilt när det gäller utsläpp av växthusgaser. Traditionellt sett har den kommersiella flygbranschen förlitat sig på konventionella bränslen baserade på flygfotogen. Tekniska framsteg i samband med ökad miljöhänsyn har lett till forskning kring Hållbara flygbränslen (SAF), med initiativ som Commercial Aviation Alternative Fuel Initiative (CAAFI) i spetsen för detta. Hållbara flygbränslen producerade från förnybara resurser som biomassa och avfall, verkar vara en lovande lösning för att minska koldioxidavtrycket från flygverksamheten. För att få ytterligare förståelse för sådana bränslen och möjliggöra implementeringen så har massvis med studier kring detta genomförts. Medan experimentella studier är viktiga är de kostsamma och tidskrävande, och därför används Computational Fluid Dynamics, CFD, för att simulera förbränning.

Detta examensarbete, genomfört i samarbete med GKN Aerospace Engine Systems, syftar till att validera förbränningsmodeller för flygbränslen med hjälp av kommersiell CFD-programvara. Studien fokuserar på att jämföra resultaten för olika förbränningsmodeller mot experimentella data, och särskilt undersöka förbränningsbeteendet och NO_x-utsläppen av både konventionellt Jet A (A2) och ett specifikt hållbart Alcohol-To-Jet (C1)-bränsle från Gevo. Studien genomförs i simuleringsverktyget STAR-CCM+, där turbulens initialt modelleras med Reynolds-Averaged Navier-Stokes (RANS) och sedan fortsätter med Large Eddy Simulation (LES). En känslighetsanalys av beräkningsnätet utförs i båda fallen, med hänsyn till turbulensens känslighet. Resultaten valideras mot referensfallet som består av experiment utförda vid Cambridge University av Pathania *et al*.

Huvudresultaten inkluderar den överlägsna prestandan hos Eddy Dissipation Concept (EDC) och Thickened Flame Model (TFM) i förbrännningssimuleringar, även om EDC-modellen visade begränsad tillämpbarhet i LES. Flamelet Generated Manifold (FGM) gav acceptabla resultat i LES för sin relativt låga beräkningskostnad. Den lilla men heltäckande reaktionsmekanismen Z79 visade bättre överensstämmelse med experimenten än HyChem-skeletalmekanismen. C1-bränslet producerade märkbart högre NO_x-utsläpp, vilket förklaras av ett högre ekvivalensförhållande och flammtemperatur. Studien belyser också den betydande påverkan av värmestrålning på simuleringens precision och förespråkar dess inkludering trots den något ökade beräkningskostnaden.

Popular Science Summary

Can Sustainable Fuels Propel Us to Greener Skies?

The aviation industry is under increasing pressure to mitigate its environmental impact, particularly concerning greenhouse gas emissions. One solution for this is using sustainable aviation fuel.

The need for sustainable and environmentally friendly fuels in existing engines is significant. More research is needed, as it is crucial to first understand these fuels complete combustion behavior and parameters. Currently, certain sustainable aviation fuels are approved for use in a 50/50 mixture with conventional fuel, as this has been proven to work well. These fuels are expensive to produce, and to gain approval for mixtures exceeding 50/50, two steps are necessary: testing different mixtures to observe their behavior and also finding a way to produce more of these fuels. As experiments are both expensive and time-consuming, it can be complementary to use quick, inexpensive, and flexible computer simulations. We have conducted computer simulations based on Computational Fluid Dynamics to identify the best existing models for predicting combustion in aircraft engines, in the commercial software STAR-CCM+. In this comparative study, four different combustion models were evaluated across distinct turbulence modeling frameworks, notably including Reynolds-Averaged Navier-Stokes and the computationally intensive Large Eddy Simulation. One notable discovery pertains to the suitability of the combustion model Eddy Dissipation Concept. While it proves to be an appropriate choice for Reynolds-Averaged Navier-Stokes simulations, its performance worsen when applied in Large Eddy Simulation. This is caused by poor software implementation of the model. Furthermore, the investigation uncovers intriguing insights into the environmental impact of different aviation fuels. Surprisingly, the sustainable aviation fuel C1 exhibits a higher propensity for nitrogen oxide, NO_x, emissions compared to the conventional Jet A fuel A2. Further studies are needed to validate this, as the equivalence ratios used for the fuels are different. Another significant revelation pertains to the computational trade-offs involved in incorporating thermal radiation into simulations. While enabling this feature enlarges the computational costs, the payoff is substantial, especially when analyzing temperature distributions or NO_x emissions. Moreover, these findings serve as a springboard for future explorations within the realm of STAR-CCM+. They provide a solid foundation for researchers to delve deeper into combustion models and reaction mechanisms.

Contents

List of Figures

List of Tables

Nomenclature

Greek Letters

α_u	Thermal diffusivity of the unburnt mixture	[m^2/s]
β	Bulk viscosity	[kg/(m·s)]
β_λ	Extinction coefficient	[-]
γ_λ	Fine structure region	[$(kg/m^3)^{0.5}$]
Γ_y	Diffusivity of progress variable	[kg/(m·s)]
δ_L	Laminar flame thickness	[m]
Δ	LES spatial filter width, Cell size	[m]
ε	Turbulence dissipation rate	[m^2/s^3]
κ	Thermal diffusivity, Reaction rate	[m^2/s, kg/(m·s^3)]
κ_f	Forward reaction rate	[kg/(m^3·s)]
κ_b	Backward reaction rate	[kg/(m^3·s)]
μ	Dynamic viscosity	[kg/(m·s)]
μ_t	Turbulence viscosity	[kg/(m·s)]
μ_0	Reference viscosity	[kg/(m·s)]
ν	Kinematic viscosity	[m^2/s]
ν_{sgs}	Subgrid-scale eddy viscosity	[m^2/s]
ρ	Density	[kg/m^3]
ρ_u	Density of the unburnt mixture	[kg/m^3]
σ_k, σ_ε, σ_t	Turbulence Prandtl numbers	[-]
σ_s	Scattering coefficient	[-]
τ	Time scale	[s]
τ_{turb}	Turbulent time scale	[s]

τ_*	Kolmogorov time scale	[s]
Υ_l^m	Spherical harmonics	[-]
φ	Transport variable	[-]
ϕ	Equivalence ratio	[-]
ϕ_{bo}	Equivalence ratio for blow-off	[-]
χ	Fraction of fine structure	[-]
ψ'	Stoichiometric coefficient for reactants	[-]
ψ''	Stoichiometric coefficient for products	[-]
ω'	Vorticity	[s^{-1}]
$\dot{\omega}_i$	Source term of species i	[kg/(m^3·s)]
$\dot{\omega}_{NO_x,prompt}$	Production rate of NO_x Prompt	[kg/(m^3·s)]
$\dot{\omega}_y$	Source term of progress variable y	[kg/(m^3·s)]
Ω	Reaction zone sensor, Solid angle	[-, sr]

Roman Letters

a	Exponent dependant on oxygen mole fraction for NO_x prompt	[-]
A	Pre-exponential factor for Prompt NO_x	[-]
A_{arr}	Pre-exponential factor for Arrhenius law	[varies]
A_1	Scattering factor	[-]
$\mathbf{b}_h$	Subgrid heat flux	[J/(m^2·s)]
$\mathbf{b}_i$	Subgrid mass flux of species i	[kg/(m^2·s)]
$\mathbf{B}$	Unresolved subgrid-scale stress	[kg/(m·s^2)]
c	Reaction progress variable	[-]
C_l	Fine structure length constant	[-]
C_p	Specific heat capacity for species i	[J/(kg·K)]
C_μ, $C_{\varepsilon 1}$, $C_{\varepsilon 2}$, C_w, C_{D1}, C_{D2}, $C_{\nu sgs}$	Model constants	[-]

$\mathbf{C}$	Courant number	[-]
cf	Correction factor	[-]
D_{bb}	Diameter of the bluff-body	[m]
D_i	Diffusion coefficient for species i	[-]
$D_{y=44mm}$	Diameter of CH_2O structure at 44 mm downstream from bluff-body	[m]
$\mathbf{D}$	Symmetric part of velocity gradient	[s^{-1}]
E	Total energy, Efficiency function	[J/kg, -]
E_a	Activation energy	[J/kg]
f	Scaling factor	[-]
$\bar{f}$	Generic instantaneous flow variable	[-]
F	LES filter, Flame thickening factor, Factor for NO_x Prompt	[-]
F_{max}	Maximum flame stretch factor	[-]
F_{max}^{loc}	Maximum flame stretch factor at each local cell	[-]
$\mathbf{F}_g$	Body force due to gravity	[kg/(m^2·s^2)]
G	Stretch factor, Incident radiation	[-, W]
h_i	Specific enthalpy for species i	[J/kg]
$h_i^{\ominus}$	Formation enthalpy for species i	[J/kg]
$\mathbf{h}$	Heat transfer rate	[J/(m^2·s)]
I	Radiative intensity, Turbulence intensity	[W/sr, -]
$I_{b\lambda}$	Black body intensity at wavelength λ	[W/sr]
I_l^m	Intensity coefficient	[-]
$I_{pb\lambda}$	Particle black body intensity at wavelength λ	[W/sr]
I_λ	Radiative intensity at wavelength λ	[W/sr]
$\mathbf{I}$	Unity tensor, Radiative intensity field	[-, W]
k	Thermal conductivity, Turbulence kinetic energy	[W/(m·K), m^2/s^2]

$k_{a\lambda}$	Absorption coefficient at wavelength λ	[-]
$k_{pa\lambda}$	Particle absorption coefficient at wavelength λ	[-]
$k_{ps\lambda}$	Particle scattering coefficient at wavelength λ	[-]
k_r	Reaction rate constant	[mol/(m^3·s)]
$k_{s\lambda}$	Scattering coefficient at wavelength λ	[-]
k_1, k_2, k_3	Reaction rate coefficients	[m^3/(kmol·s)]
L	Turbulence length scale	[m]
L_T	Integral length scale	[m]
M	Total number of reactions	[-]
MW_i	Molar weight of species i	[kg/mol]
MW_k	Molar weight of species k	[kg/mol]
MW_{NO_x}	Molar weight of NO$_x$	[kg/mol]
n	Temperature exponent	[-]
N	Total number of species, Total number of cells in flame	[-]
p	Pressure	[Pa, atm]
P_k	Production of turbulence kinetic energy	[kg/(m·s^3)]
Pr	Prandtl number	[-]
q_j	Rate of progress of a specific reaction j	[kg/(m^3·s)]
$\dot{q}_c$	Heat release from chemical reactions	[J/(m^3·s)]
$\mathbf{q}$	Radiative heat flux	[J/s]
$\mathbf{r}$	Specific point within medium	[m]
R	Universal gas constant	[J/(mol·K)]
$R_{i,kin}$	Chemical kinetic reaction rate for species i	[s^{-1}]
s	Distance	[m]
$\hat{\mathbf{s}}$	Direction unit vector	[-]

S	Sutherland constant	[K]
S_{ij}	Resolved strain rate tensor	[s^{-1}]
S_{ij}^d	Symmetric traceless part of the square of the velocity gradient tensor	[s^{-2}]
S_L	Laminar flame speed	[m/s]
S_t	Turbulent flame speed	[m/s]
$\bar{\mathbf{S}}$	Viscous stress tensor	[kg/(m·s^2)]
Sc_i	Schmidt number for species i	[-]
t	Time	[s]
Δt	Time-step	[s]
T	Temperature	[K]
T_0	Reference temperature	[K]
u	Velocity	[m/s]
u'	Turbulent velocity	[m/s]
U_b	Bulk velocity	[m/s]
$\mathbf{v}$	Fluid velocity vector	[m/s]
$\mathbf{x}$	Location vector	[m]
$\mathbf{x}'$	Location vector for the fluctuating components	[m]
Δx	Cell size in x-direction	[m]
X_i	Concentration of species i	[mol/m^3]
y	Unnormalized reaction progress variable	[-]
y_b	Unnormalized reaction progress variable at burnt state	[-]
y_{mean}	Averaged unnormalized reaction progress variable	[-]
y_u	Unnormalized reaction progress variable at initial unburnt state	[-]
Y_i	Mass fraction of species i	[-]
Y_k	Mass fraction of species k	[-]

Y_i^0	Mass fraction of species i for surrounding structure region	[-]
Y_i^*	Mass fraction of species i for fine structure region	[-]
Y_i^τ	Mass fraction of species i at the end of time integration	[-]
$\mathbf{Y}$	Mass fraction vector	[-]

Operations

$\bar{\phi}$	Filtered
$\tilde{\phi}$	Favre averaged
∇	Nabla operator (gradient)
$\nabla\cdot$	Nabla operator (divergence)
$\nabla \cdot \nabla = \nabla^2$	Laplacian
$\otimes$	Kronecker product
$\langle\phi\rangle$	Time-averaged

Abbreviations

AFR	Air-To-Fuel ratio
ATJ	Alcohol-To-Jet
BC	Boundary Condition
BP-TR	Broadened Preheat Thin Reactions
CAAFI	Commercial Aviation Alternative Fuel Initiative
CFD	Computational Fluid Dynamics
CVODE	C-language Variable-coefficients Ordinary Differential Equation
EDC	Eddy Dissipation Concept
FGM	Flamelet Generated Manifold
FRC	Finite Rate Chemistry
FSCK	Full Spectrum Correlated-k
FSD	Flame Surface Density

HyChem	Hybrid Chemistry
LES	Large Eddy Simulation
LFC	Laminar Flame Concept
LTH	Lunds Tekniska Högskola, The Faculty of Engineering at Lund University
NJFCP	National Jet Fuel Combustion Program
NSE	Navier-Stokes Equation
NTC	Negative Temperature Coefficient
ODE	Ordinary Differential Equation
PaSR	Partially Stirred Reactor
PFP	Premixed Freely Propagating
PISO	Pressure-Implicit with Splitting of Operators
PIV	Particle Image Velocimetry
PLIF	Planar Laser-Induced Fluorescence
PSR	Perfectly Stirred Reactor
RANS	Reynolds-Averaged Navier-Stokes
RTE	Radiative Transfer Equation
SAF	Sustainable Aviation Fuel
SGS	Subgrid-scale
TFC	Turbulent Flame Speed Closure
TFM	Thickened Flame Model
T-F	Thin Flamelets
WALE	Wall-Adapting Local Eddy-Viscosity
WSGG	Weighted Sum of Grey Gases
ZG	Zero-gradient

1 Introduction

In recent decades, the aviation industry has faced increasing pressure to address its environmental footprint. With concerns over climate change and the urgency to reduce greenhouse gas emissions, the quest for sustainable solutions has become imperative. Among the array of strategies aimed at mitigating the environmental impact of aviation, the adoption of sustainable aviation fuels (SAF) has emerged as a promising avenue.

SAFs, derived from renewable resources such as biomass, waste oils, and synthetic processes, offer the potential to significantly reduce the carbon intensity of aviation operations compared to conventional fossil fuels. As the aviation sector strives to transition towards a more sustainable future, understanding the viability, challenges, and implications of integrating SAFs into existing infrastructures becomes paramount.

This master's thesis aims to validate the current combustion modeling of aviation fuels using commercial software based on Computational Fluid Dynamics (CFD). It is carried out in collaboration with GKN Aerospace Engine Systems in Trollhättan, Sweden. The company produces components for aircraft engines globally and has the mission to be the most trusted and sustainable partner in the sky [1].

1.1 Background

Throughout the history of aviation, the commercial industry has been using only a few different, but well-proven, conventional fuels for the operation of aircraft engines. For turbine-powered aircraft, conventional kerosene-based fuels have been used [2]. The National Jet Fuel Combustion Program (NJFCP), has introduced three categories for reference fuels to facilitate research and enable the broader adoption of bio-jet fuels with increased blending limits [3]. Category A consists of conventional fossil-derived fuels, such as Jet A (A2), Jet A-1, JP-5, and JP-8. Category B consists of fuels with undesirable thermophysical and combustion characteristics, while C consists of test fuels that are at the boundaries of feasible characteristics [4].

The Commercial Aviation Alternative Fuel Initiative (CAAFI) coalition was established in 2006 to advance the development and utilization of sustainable aviation fuels. This initiative emerged in response to supply and security issues, and environmental concerns associated with petroleum. In recent decades, synthetic aviation fuel derived from biomass has been investigated. Rumizen [2] explains the different pathways to synthesize SAF from specific biomass sources. ASTM D7566 is a standard for the blending of SAF in conventional jet fuel [5]. The standard currently holds nine approved pathways for different processes that can be used and blended up to a certain amount (10-50%). One approved pathway for producing bio-jet fuel is Alcohol-To-Jet (ATJ). One such ATJ, from Gevo, is denoted C1 and is considered to be renewable as compared to conventional jet fuel [4]. Other pathways for producing synthetic paraffinic kerosene include gasification of coal or biomass by using

a Fischer-Tropsch process, hydro-processing of esters and fatty acids, and processing of fermented sugars [2]. The two former may be blended up to 50% by volume along with Jet A, just as C1, while the latter is limited to 10%. When the blending has been made, another standard is applied, the ASTM D1655, which makes the blend a Jet A fuel independent of the origin.

The initiative RefuelEU Aviation is a central part of the EU's "fit for 55" package, which seeks to reduce net greenhouse gas emissions by at least 55% by 2030. RefuelEU aims to boost both the demand for and the supply of sustainable aviation fuels while ensuring equal conditions for the EU's aviation market [6]. By 2025, the fuel supplier is required to include an average of 2% SAF in their supplied fuels, with this requirement rising to 6% by 2030.

In 2021, an experimental study at Cambridge University was performed regarding premixed bluff-body stabilized flames operated with vaporized liquid jet fuels [7]. The fuels were ethanol, heptane, Jet A, and C1. The objective of the study was to, via Planar Laser-Induced Fluorescence (PLIF) imaging of hydroxyl radical, OH, and formaldehyde, CH_2O, provide comparisons between the structures of such flames in two operating conditions, one far from blow-off, and one close to blow-off. Numerous studies have explored the differences in the chemical and physical characteristics between conventional jet fuel and sustainable aviation fuel. The growing need to reduce emissions drives this research to enable more SAF use in existing engines. Computational Fluid Dynamics can be an effective tool for facilitating quicker and more cost-effective testing. However, to ensure that the simulations are comparable to an experimental study, several validation processes are necessary. These can include testing various reaction mechanisms, combustion models, and additional models, such as NO_x emissions or thermal radiation.

1.2 Benchmark

The benchmark case for this study is the experiment conducted at Cambridge by Pathania *et al.* [7]. In their setup, a burner featuring a 23 mm diameter bluff-body mounted on a 6.5 mm rod, as depicted in Figure 1.1, was utilized. A premixed air-fuel mixture, with a bulk velocity, U_b, of 23.5 m/s, entered through a 35 mm diameter annular opening. The fuels examined in the benchmark case include A2, C1, ethanol, and n-heptane. Two inlet conditions based on equivalence ratio, ϕ , were investigated: one far from blow-off (ϕ/ϕ_{bo} = 1.2) and one close to blow-off (ϕ/ϕ_{bo} = 1.01). PLIF imaging was used for OH and CH_2O visualization to study the effect of fuel composition. It is worth noting that the radical concentrations are not quantified in this type of imaging method.

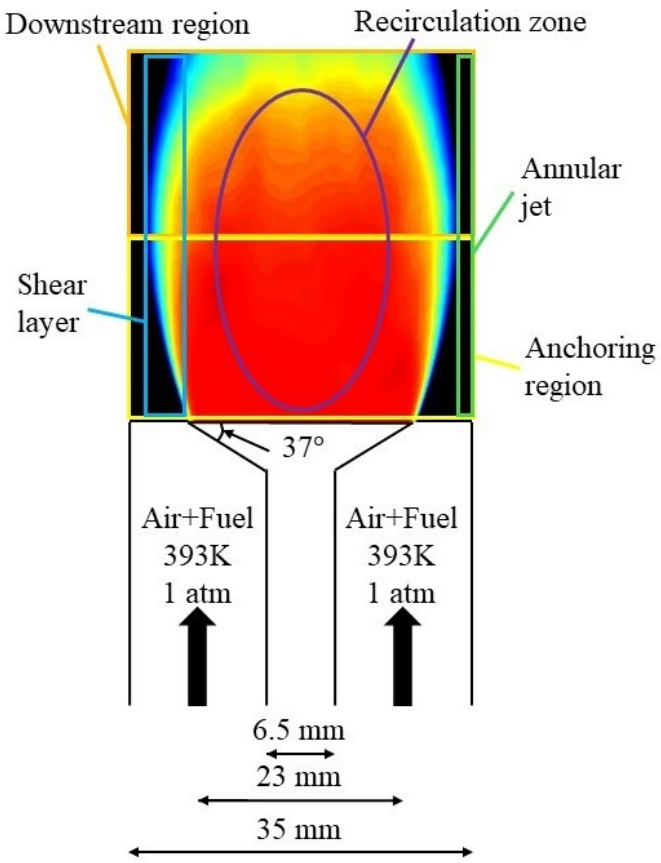

Figure 1.1: Schematic of bluff-body burner and the regions of the flame, reproduced from Pathania *et al.* [7], where the bluff-body angle was not given.

Although the angle of the bluff-body is not specified in the article, it was decided, following consultation with the supervisor, to set it at 37°.

1.3 Aim

The aim of this work is fourfold:

- To validate the chosen combustion models, which are implemented in the software STAR-CCM+, as a simulation tool for premixed bluff-body stabilized flames using Jet A (A2) and sustainable aviation fuel C1.
- To compare the HyChem skeletal reaction mechanism by Stanford University [8] [9] [10] and Z79 reaction mechanism by Zettervall [11], designed for A2 and C1, in the context of premixed combustion.
- To study and compare the NO_x emissions during combustion of A2 and C1.
- Finally, to study the effects of thermal radiation.

2 Theory

This chapter commences with an overview of the key physical phenomena of premixed flames. Following this overview, a series of the governing equations are introduced to encapsulate the interplay between flow dynamics and chemical physics within premixed flames. These equations serve as the foundation for understanding the physics at work. To complement the governing equations, a comprehensive set of constitutive equations and turbulence models are presented to set up the framework to use Computational Fluid Dynamics. To enable the simulation and analysis of turbulent flames, additional modeling of turbulence-chemistry interaction is necessary. Various approaches for accomplishing this task are presented.

2.1 Premixed Flame

Premixed combustion refers to a flame front propagating in a mixture of fresh reactants composed of air and fuel, with burnt products behind the flame front [12]. In a laminar flow field, the flame front propagates with a velocity called laminar flame speed, S_L, and has a thickness, δ_L, in the order of 0.1 mm, both of which are determined by the fuel composition and the initial conditions. In a turbulent flow field, the flame becomes wrinkled as the flame front interacts with the turbulent eddies which increases the mixing between burnt and unburnt regions and increases the consumption rate and the overall thickness of the flame front. The structure of a premixed flame can be explained by an unburnt zone, a preheat zone, a reacting zone, and a post-flame zone [12]. The unburnt zone is characterized by only having reactants and the post-flame zone by only having products. The reacting zone has a mix of reactants and products and it is congruent with the flame front. The preheat zone is just before the flame front where the initial reactions have begun due to increased temperature. Some molecules, also known as radicals, are present in large concentrations in specific zones, which can indicate the location of the flame zones. These include formaldehyde, CH_2O, which is predominant in the preheat zone, and hydroxyl radical, OH, which is predominant in the reacting zone.

In bluff-body stabilized flames, instabilities in the flame front can arise at the interface between two fluids moving in different directions or at different velocities. Known as Kelvin-Helmholtz instabilities [13], these can result in interfacial roll-ups, vortices, and small-scale turbulence. A recirculation zone forms downstream of the bluff-body, and the aforementioned instabilities are observed in the shear layer of this recirculation region.

2.2 Governing Equations

In fluid dynamics and heat transfer, the governing equations are the fundamental principles that describe the behavior of fluids and their interactions with heat and other constituents. In

the case of combustion, the governing equations typically consist of at least four equations. These will be described below, and together they form the reacting Navier-Stokes equations (NSE) [14].

2.2.1 Continuity equation

The continuity equation, also known as the conservation of mass, describes that mass can neither be created nor destroyed within a system. It is expressed as [15]

$$\frac{\partial \rho}{\partial t} + \nabla \cdot (\rho \mathbf{v}) = 0 \tag{2.1}$$

where

ρ is the fluid density,
$\mathbf{v}$ is the fluid velocity vector, and
t is the time.

2.2.2 Momentum Equation

The momentum equation describes the relationship between forces acting on a fluid and its resulting acceleration. It is expressed as [15]

$$\frac{\partial (\rho \mathbf{v})}{\partial t} + \nabla \cdot (\rho \mathbf{v} \otimes \mathbf{v}) = -\nabla p + \nabla \cdot \left((\beta - \frac{2}{3}\mu) \nabla \cdot \mathbf{v} \mathbf{I} + 2\mu \mathbf{D} \right) + \mathbf{F}_g \tag{2.2}$$

where

p is the pressure,
$\mathbf{I}$ is the unity tensor,
β is the bulk viscosity, and according to Stokes' hypothesis is set to zero [12],
μ is the dynamic viscosity,
$\mathbf{D}$ is the symmetric part of the velocity gradient, and
$\mathbf{F}_g$ is the body force due to gravity.

2.2.3 Energy Equation

The energy equation describes the transfer of thermal energy within a fluid and its surroundings. It is expressed as [15]

$$\frac{\partial \rho E}{\partial t} + \nabla \cdot (\rho \mathbf{v} E) = -\nabla \cdot (\mathbf{v} \cdot p) + \nabla \cdot \left(\left((\beta - \frac{2}{3}\mu)(\nabla \cdot \mathbf{v}) \mathbf{I} + 2\mu \mathbf{D} \right) \cdot \mathbf{v} + k \nabla T \right) + \dot{q}_c \tag{2.3}$$

where

E is the total energy,
k is the thermal conductivity,
T is the temperature, and
$\dot{q}_c$ is the heat release from chemical reactions.

The heat release is defined as

$$\dot{q}_c = \sum_{i=1}^{N} h_i^{\ominus} \dot{\omega}_i \tag{2.4}$$

where

N is the total number of species,
$h_i^{\ominus}$ is the formation enthalpy for species i, and
$\dot{\omega}_i$ is the species production rate.

2.2.4 Species Equation

The species equation describes the transport of chemical species within a fluid. For species *i* it is expressed as [15]

$$\frac{\partial \rho Y_i}{\partial t} + \nabla \cdot (\rho \mathbf{v} Y_i) = \nabla \cdot (D_i \nabla Y_i) + \dot{\omega}_i \tag{2.5}$$

where

Y_i is the mass fraction of species i, and
D_i is the diffusivity.

2.2.5 The Reacting Flow Equations Combined

To make referencing easier, the governing equations are given below. Together they form the reactive NSE

$$\begin{cases} \dfrac{\partial \rho}{\partial t} + \nabla \cdot (\rho \mathbf{v})) = 0 & \text{(2.6a)} \\ \dfrac{\partial (\rho \mathbf{v})}{\partial t} + \nabla \cdot (\rho \mathbf{v} \otimes \mathbf{v})) = -\nabla p + \nabla \cdot \left((\beta - \dfrac{2}{3}\mu) \nabla \cdot \mathbf{v} \mathbf{I} + 2\mu \mathbf{D} \right) + \mathbf{F}_g & \text{(2.6b)} \\ \dfrac{\partial \rho E}{\partial t} + \nabla \cdot (\rho \mathbf{v} E) = -\nabla \cdot (\mathbf{v} \cdot p) + \nabla \cdot \left(\left((\beta - \dfrac{2}{3}\mu)(\nabla \cdot \mathbf{v}) \mathbf{I} + 2\mu \mathbf{D} \right) \cdot \mathbf{v} + k \nabla T \right) + \dot{q}_c & \text{(2.6c)} \\ \dfrac{\partial \rho Y_i}{\partial t} + \nabla \cdot (\rho \mathbf{v} Y_i) = \nabla \cdot (D_i \nabla Y_i) + \dot{\omega}_i & \text{(2.6d)} \end{cases}$$

2.3 Constitutive Equations

The equations employed for closing the NSE serve to incorporate physical laws and additional variables, such as temperature, into the NSE framework [15]. Constitutive equations describe how the fluid mixture responds to external forces. In many practical scenarios, the flow can be approximated as a Newtonian fluid, exhibiting Fourier heat conduction and Fickian diffusion. The dynamic viscosity, denoted by μ, adheres to Sutherland's Law, expounded upon in Section 2.3.1. Furthermore, the species and thermal diffusivities are

modeled as $D_i = \rho\nu/Sc_i$ and $\kappa = \mu/Pr$, respectively, where ν denotes kinematic viscosity, Sc_i denotes the Schmidt number for species i, and Pr denotes the Prandtl number.

Another assumption often applied for general flow simulation is the ideal gas law, which relates the pressure to the density and temperature, and is given by [12]

$$p = \sum_i (\rho_i) \left(\sum_i Y_i \frac{R}{MW_i} \right) T \tag{2.7}$$

where

R is the universal gas constant, and
MW_i is the molar weight of species i.

The heat transfer rate, **h**, is modeled using Fourier heat conduction expressed using thermal conductivity k as [15]

$$\mathbf{h} = -k\nabla T, \quad k = k(T, Y_i) \tag{2.8}$$

where k is a function of temperature and mass fraction.

2.3.1 Sutherland's Law

When solving the flow equations viscosity can either be assumed constant, or modeled based on parameters such as temperature. A constant viscosity assumption is often used and can give accurate results when the temperature fluctuations in the domain are low. In a reactive flow case, however, it is ill-advised since the temperature will fluctuate substantially between unburnt and burnt regions. One way to model the viscosity is Sutherland's Law [16], which relates the viscosity to the temperature, and is given by

$$\mu(T) = \mu_0 \left(\frac{T}{T_0} \right)^{\frac{3}{2}} \frac{T_0 + S}{T + S} \tag{2.9}$$

where

$\mu(T)$ is the dynamic viscosity at temperature T,
μ_0 is the reference viscosity at reference temperature T_0, and
S is the Sutherland constant.

Sutherland's Law is an old and heavily corroborated model that can approximate the viscosity with a margin of error of a few percent [16].

2.4 Finite Volume Method

To solve the reactive NSE given in Section 2.2.5 certain approximations are necessary due to their nonlinear and continuous nature. By discretizing the equations into a finite number

of elements, numerical solutions can be obtained by assuming linear behavior within each discrete domain. In CFD the most common way to do so is to use the finite volume method, as it has the benefit of keeping the mass conserved even after discretizing. The method includes integrating the NSE over the control volume and applying the divergence theorem to convert volume integrals to surface integrals of fluxes. Subsequently, the discretization of the domain is performed spatially and temporally. This then makes it possible to solve the NSE by considering the initial and boundary conditions and the convective and diffusive fluxes between the discretized cells [14]. This renders the nonlinear Navier-Stokes equations linear within a discrete domain. This approach does, however, introduce numerical error in the solution which in theory approaches zero when the cell size is reduced. Therefore a mesh sensitivity study might be necessary to show that a reduction in cell size does not impact the results.

2.4.1 Courant Number

Reducing cell size has negative effects, however, and to illustrate it the Courant number [17] is used which is given by

$$\mathbf{C} = u\frac{\Delta t}{\Delta x} \tag{2.10}$$

where

Δt is the time-step, and
Δx is the cell size in the x-direction.

It is dimensionless and represents the number of mesh cells a fluid has traveled in a given time-step. It is used in the Courant-Friedrichs-Lewy, or CFL condition to measure how long the time-step can be for a given mesh size. For an explicit solver, the Courant number should not be larger than 1 to avoid instabilities and keep the accuracy high. This means that to keep the solver stable when reducing cell size the time-step also has to be reduced, increasing the computational costs. Meanwhile, an implicit solver is unconditionally stable for unreacting flow, thus making CFL condition irrelevant to the stability of the flow simulation. For reacting flow simulations, however, the chemistry can become unstable with a longer time-step.

2.5 Chemical Kinetics

Essentially, chemical kinetics is the study of reaction rates. The chemical kinetics determines how long it takes for a system to reach its final equilibrium state. Certain properties of a given fuel such as the laminar flame speed and ignition delay time are included in the chemical kinetics of a given system and can give some insight into the behavior of the system.

2.5.1 Laminar Flame Speed

Laminar flame speed, S_L, describes how fast the flame front propagates relative to the unburnt mixture [12]. This is an important property of a premixed flame because it holds fun-

damental information about the diffusivity, reactivity, and exothermicity of the combustible hydrocarbon mixture. Practically speaking, laminar flame speed is related to the combustion speed in the combustion chamber, which can affect the combustion efficiency [18]. The laminar flame speed is dependent on the fuel, fuel concentration in the mixture, and the initial temperature and pressure.

2.5.2 Reaction Mechanisms

A reaction mechanism describes how a chemical reaction proceeds step by step. The mechanisms can be of various levels of detail; on the one hand, they can be detailed enough to describe several of the small sub-reactions that take place before the system has reached its final equilibrium state [14]. On the other hand, they can be simplified and made more practically useful by involving fewer sub-reactions and thereby also fewer species [19]. It has been common practice to use global reaction mechanisms in CFD, involving only a few reactions and species. In recent years, the simplification of detailed reaction mechanisms into skeletal form, which can consist of only a few reactions to several hundred, has become increasingly prevalent. This is supported by the demonstrated higher accuracy and the advancements in computational power. To simulate the reactions, the rate of progress q_j of a specific reaction j is necessary, and given as [11]

$$q_j = \kappa_{fj} \prod_{i=1}^{N} [X_i]^{\psi'_{ij}} - \kappa_{rj} \prod_{i=1}^{N} [X_i]^{\psi''_{ij}} \tag{2.11}$$

where

κ_f and κ_r are the forward and backward reaction rates, respectively,
X_i is the concentration of species i, and
ψ' and ψ'' are stoichiometric coefficients for reactants and products, respectively.

The reaction rate κ in equation 2.11 is calculated from a modified Arrhenius law as [11]

$$\kappa = A_{arr} T^n exp\left(-\frac{E_a}{RT}\right) \tag{2.12}$$

where

A_{arr} is the pre-exponential factor,
n is the temperature exponent, and
E_a is the activation energy.

The rate of production, $\dot{\omega}_i$, of species i can then be calculated as [11]

$$\dot{\omega}_i = \sum_{j=1}^{M} \left(\psi''_{ij} - \psi'_{ij}\right) q_j \tag{2.13}$$

where M is the number of reactions.

2.6 Turbulence Modeling

Turbulence can be regarded as one of the most important unsolved problems in classical physics to this day. It has been researched for decades, and it still lacks a general analytical theory capable of predicting the evolution of turbulent flows. Therefore, turbulence modeling is needed to evaluate the effects of turbulence.

2.6.1 Reynolds-Averaged Navier-Stokes

RANS is a method for predicting turbulence effects on the mean flow. It does not resolve the details of the turbulent fluctuations but rather averages the properties of the flow over time. Many important properties such as the fluctuating velocity components are lost in the time-averaging but in most engineering applications RANS simulations give enough information based on the mean flow data. Due to omitting the fluctuating parts of velocity new unknown terms called Reynolds stresses emerges, which can be modeled using the Boussinesq assumption [20]. A two equation model can then be used to calculate the turbulent viscosity, needed for the modeling. RANS can be used with a steady-state assumption, or transiently to capture unsteady temporal effects.

One model that closes the mean flow is the so-called $k-\varepsilon$ model which includes two extra transport equations to be solved along with the RANS flow equations [14], the turbulence kinetic energy, k, and the turbulence dissipation rate, ε. The fundamental assumption for the two equation models is that the turbulence is locally isotropic which would infer that the nondiagonal elements of the Reynolds-Stress matrix are zero, and that the diagonal elements are equal to each other. Then the entire Reynolds-Stress matrix can be modeled with one transport equation, k. The $k-\varepsilon$ turbulence model transport equations are given by [14]

$$\begin{cases} \frac{\partial(\rho k)}{\partial t} + \nabla \cdot (\rho \langle u \rangle k) = \nabla \cdot [(\mu + \sigma_k \mu_t) \nabla k] + P_k - \rho\varepsilon \\ \frac{\partial(\rho \varepsilon)}{\partial t} + \nabla \cdot (\rho \langle u \rangle \varepsilon) = \nabla \cdot [(\mu + \sigma_\varepsilon \mu_t) \nabla \varepsilon] + C_{\varepsilon 1} \frac{\varepsilon}{k} P_k - C_{\varepsilon 2} \rho \frac{\varepsilon^2}{k} \end{cases} \tag{2.14}$$

where

k is the turbulence kinetic energy,
ε is the turbulence dissipation rate,
μ_t is the turbulence viscosity and given by $\mu_t = \rho C_\mu k^2/\varepsilon$,
P_k is the production of turbulence kinetic energy,
σ_k and σ_ε are turbulence Prandtl numbers, and
$C_\mu, C_{\varepsilon 1}$ and $C_{\varepsilon 2}$ are model constants.

2.6.2 Large Eddy Simulation

In LES as compared to RANS, most of the turbulent scales are resolved and only the small-scale turbulence is modeled using a subgrid-scale model [15]. The range of the turbulent scales that are resolved is decided with a spatial filter, Δ. In CFD this filter is usually the same as the cell size. To resolve all turbulent scales the cell size has to be very small which makes the simulation expensive, for most purposes, it is common to assume that about 80%

of the turbulence kinetic energy should be resolved and the rest can be modeled to have a sufficiently refined LES [20]. As mentioned, a spatial low-pass filter is used to resolve the largest turbulent eddies, and unlike RANS equations, the LES equations are solved for the filtered values instead of the averaged ones. The filtering of a generic instantaneous flow variable $\bar{f}(t, \mathbf{x})$ is defined as [12]

$$\bar{f}(\mathbf{x}) = \int f(\mathbf{x}')F(\mathbf{x} - \mathbf{x}')d\mathbf{x}' \tag{2.15}$$

where

$\mathbf{x}$ is the location vector,
$\mathbf{x}'$ is the location vector for the fluctuating components, and
F is the LES filter.

For variable density, a mass-weighted Favre filtering is introduced as [12]

$$\bar{\rho}\tilde{f}(\mathbf{x}) = \int \rho f(\mathbf{x}')F(\mathbf{x} - \mathbf{x}')d\mathbf{x}' \tag{2.16}$$

After filtering the NSE in Section 2.2.5 the resulting LES equations are [15]

$$\begin{cases} \dfrac{\partial \bar{\rho}}{\partial t} + \nabla \cdot (\bar{\rho}\widetilde{\mathbf{v}}) = 0 & \text{(2.17a)} \\ \dfrac{\partial (\bar{\rho}\widetilde{\mathbf{v}})}{\partial t} + \nabla \cdot (\bar{\rho}\widetilde{\mathbf{v}} \otimes \widetilde{\mathbf{v}}) = -\nabla \bar{p} + \nabla \cdot (\bar{\mathbf{S}} - \mathbf{B}) + \mathbf{F}_g & \text{(2.17b)} \\ \dfrac{\partial (\bar{\rho}\widetilde{E})}{\partial t} + \nabla \cdot (\bar{\rho}\widetilde{\mathbf{v}}\widetilde{E}) = -\nabla \cdot (\widetilde{\mathbf{v}} \cdot \bar{p}) + \bar{\mathbf{S}} \cdot \nabla \widetilde{\mathbf{v}} + \nabla \cdot (\kappa \nabla \widetilde{T} - \mathbf{b}_h)) + \bar{\dot{q}}_c & \text{(2.17c)} \\ \dfrac{\partial \bar{\rho}\widetilde{Y_i}}{\partial t} + \nabla \cdot (\bar{\rho}\widetilde{\mathbf{v}}\widetilde{Y_i}) = \nabla \cdot (\dfrac{\mu}{Sc_i}\nabla \widetilde{Y_i} - \mathbf{b}_i) + \bar{\dot{\omega}}_i & \text{(2.17d)} \end{cases}$$

where $\bar{}$ and $\widetilde{}$ denotes filtered and Favre filtered variables, respectively. The viscous stress tensor $\bar{\mathbf{S}}$ is

$$\bar{\mathbf{S}} = \left((\beta - \frac{2}{3}\mu)\nabla \cdot \widetilde{\mathbf{v}}\mathbf{I} + 2\mu\widetilde{\mathbf{D}} \right) \tag{2.18}$$

and the unresolved subgrid stress and flux terms are $\mathbf{B} = \bar{\rho}(\widetilde{\mathbf{v} \otimes \mathbf{v}} - \widetilde{\mathbf{v}} \otimes \widetilde{\mathbf{v}})$, $\mathbf{b}_i = \bar{\rho}(\widetilde{\mathbf{v}Y_i} - \widetilde{\mathbf{v}}\widetilde{Y_i})$ and $\mathbf{b}_h = \bar{\rho}(\widetilde{\mathbf{v}E} - \widetilde{\mathbf{v}}\widetilde{E})$. To close the filtered equations the subgrid stress and flux terms $\mathbf{B}$, $\mathbf{b}_i$ and $\mathbf{b}_h$ have to be modeled.

LES is appropriate for resolving turbulence which generally gives more information than the RANS approach, but it comes with drawbacks. LES has to be used transiently and in 3D which adds to the computational cost. It is also less validated than most RANS models [19].

2.6.2.1 Subgrid-Scale Model

The turbulence in LES is divided into resolved and unresolved turbulence depending on the filter width, Δ, as previously mentioned. This means that a model needs to be applied

to predict the small-scale turbulence that is unresolved. There have been several different approaches to modeling the subgrid-scale based on Boussinesq eddy viscosity assumption [20], to model the subgrid-scale stress term, **B**. This assumption holds more validity in modeling subgrid turbulence because it tends to be more isotropic compared to turbulence at larger scales. One of the common subgrid-scale models is the Smagorinsky model which uses an equation for the subgrid eddy viscosity, ν_t, to estimate the effects of turbulence by increasing viscosity at the subgrid-scale [20]. For this study another common model was chosen—the so-called WALE model, Wall-Adapting Local Eddy-viscosity which is similar to the Smagorinsky model but often used in LES of turbulent flows when wall effects are of more concern. It was first introduced in 1999 by Nicoud and Ducros [21] as an attempt to improve the performance of LES in near-wall regions, where the Smagorinsky model often struggles due to its inability to accurately capture near-wall effects. The equation is given as [21]

$$\nu_{sgs} = (C_w \Delta)^2 \frac{(S_{ij}^d S_{ij}^d)^{3/2}}{(S_{ij} S_{ij})^{5/2} + (S_{ij}^d S_{ij}^d)^{5/4}} \tag{2.19}$$

where

ν_{sgs} is the subgrid-scale eddy viscosity,
C_w is a model constant, typically between 0.5 and 0.6,
S_{ij} is the resolved strain rate tensor, and
S_{ij}^d is the symmetric traceless part of the square of the velocity gradient tensor.

This formulation of the eddy viscosity takes both the local strain and the rotational rate into account, thus all turbulence structures relevant for the kinetic energy dissipation are detected by the model [21]. For further information refer to [14] and [21].

2.7 Turbulence-Chemistry Interaction

Turbulence-chemistry interaction refers to precisely what its name suggests: a method that efficiently handles both the characteristics of turbulence and the kinetic interaction between turbulence and chemistry [22]. Turbulent combustion is not trivial to simulate as different time scales, both turbulent and chemical, vary over a wide range [12]. It is not advisable to resolve all time scales in a simulation due to high computational cost, and therefore LES has been designed to filter the turbulence to only resolve the larger scales. Since the filter excludes smaller eddies and time scales where the majority of chemical interactions occur within turbulence, an additional model must be implemented to address this issue.

Numerous models are available with a range of applications and effectiveness, categorized broadly into two main groups—Finite Rate Chemistry (FRC) models and Flamelet models. Because of the scope of this thesis, it is limited to what has been implemented in STAR-CCM+. Among the FRC models, three chosen models are included in the study: Laminar Flame Concept (LFC), Eddy Dissipation Concept (EDC), and Thickened Flame Model (TFM). From the Flamelet models, one is included, Flamelet Generated Manifold (FGM).

2.7.1 Finite Rate Chemistry

FRC is a direct method for implementing combustion chemistry in CFD simulations [23]. It refrains from making assumptions about the flow or flame. Instead, it uses a Arrhenius expression to calculate the reaction rate, and solve the species equations by solving the chemistry ODE in each cell at every time-step [19].

2.7.1.1 Laminar Flame Concept

The Laminar Flame Concept represents one approach to utilizing FRC, presuming a laminar flame and disregarding turbulent influences. Essentially, it treats the cells as homogeneously mixed reactors, solved via an ODE to track the evolution of reaction species over time. In this model, flame attributes are solely determined by chemical kinetics.

2.7.1.2 Eddy Dissipation Concept

EDC is based on the energy cascade model, which states that energy transitions from bigger to smaller turbulent structures [22]. In Figure 2.1, a few structure levels of the energy cascade process are schematically illustrated. Turbulence kinetic energy, denoted as k, primarily originates in large-scale eddies through interaction with the mean flow. During this process, mechanical energy transfers from large-scale structures to smaller-scaled structures, accompanied by heat release. This sequence repeats across several intermediate structure scales, simplistically grouped as ”Intermediate-structure scales” in the schematic. At each level, mechanical energy from the preceding structure is inherited, leading to further heat dissipation. This cycle persists until reaching the small-scale structures, closely related to the Kolmogorov scales, where all remaining energy dissipates into heat. At each structure level, the vorticity, ω', is changed. For more specific information on this, refer to [22].

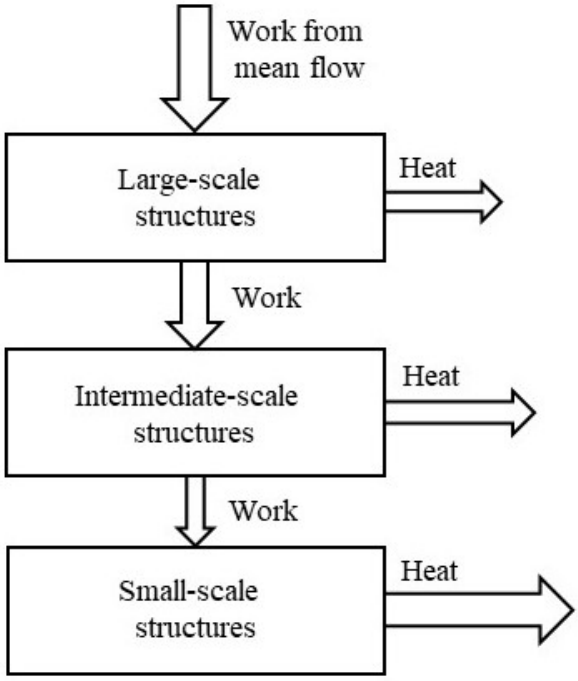

Figure 2.1: Schematic of energy cascade.

In 2005 it was concluded by Magnussen [22] that chemical reactions may occur in both the small-scale structures, also denoted as fine structures, and in the surroundings. Fast thermal reactions will occur exclusively within the confines of the fine structure regions, but in the case of slow reactions, the reaction zone may extend beyond the confines of the fine structure regions, reaching into the surrounding fluid. For detailed chemistry, the mixing rate within the fine structure regions is much faster than the exchange rate to the surrounding fluid, and therefore the fine structure regions are treated as a Perfectly Stirred Reactor (PSR), which assumes that the reactants are homogeneously mixed [24].

To model the filtered reaction rates, Magnussen [22] proposed the following source term for the species transport equation [25]

$$\dot{\omega}_i = \frac{\gamma_\lambda^2 \chi}{\tau_*}(Y_i^0 - Y_i^*) \tag{2.20}$$

where $\frac{\gamma_\lambda^2}{\tau_*}$ is the mass exchange between surrounding and fine structure region and χ is the fraction of the fine structure where the reaction takes place, and it is unity for detailed kinetics. The superscripts ^{0} and * denote surrounding and fine structure regions.

The fine structure region can be expressed as $\gamma_\lambda = (\frac{3C_{\nu sgs}C_{D2}}{4C_{D1}^2})^{1/4}(\frac{\nu}{\nu_{sgs}})^{1/4}$ where C_{D1}, C_{D2} and $C_{\nu sgs}$ are model constants [25]. The mixing time scale for RANS, τ_* is evaluated using Kolmogorov time scale as $\tau_* = (\frac{C_{D2}}{3})^{0.5}(\frac{\nu}{\varepsilon})^{0.5}$. In an LES simulation the eddy dissipation, ε, should be evaluated as $\varepsilon = 2(\nu_{sgs} + \nu)|\widetilde{S}|^2$ according to Panjwani *et al.* [25].

2.7.1.3 Thickened Flame Model

The flame front of a turbulent premixed flame is too thin to efficiently resolve it on a mesh. Therefore, the Thickened Flame Model is developed to artificially thicken the flame to resolve the flame front on the computational grid [12]. This is performed by increasing the diffusivity by a factor F and lowering the reaction rate by the same factor, effectively keeping the laminar flame speed constant. A drawback in the static TFM is that the diffusion is scaled in the whole domain which can lead to errors in mass fraction prediction. To overcome this, a modified version was presented that identifies the flame zone by a sensor, Ω. It is based on either reaction rate or progress variable [26], and only increases the diffusivity in that area instead of the entire domain. After thickening the flame the surface area of the flame is reduced, and to compensate for this an efficiency function E is introduced. It is evaluated as the ratio of a wrinkling factor of the flame before and after artificially thickening the flame, yielding an E larger than 1.

The modified transport equation for TFM is given as

$$\frac{\partial \rho \varphi_i}{\partial t} + \nabla \cdot (\rho \mathbf{v} \varphi_i) = \nabla \cdot \left[\left(DEF + \frac{\mu_t}{\sigma_t}(1-\Omega) \right) \nabla \varphi_i \right] + \frac{E}{F} \dot{\omega}_i \tag{2.21}$$

where

φ is the transport variable,
D is the diffusion coefficient,
E is the efficiency factor,
F is the flame thickening factor,
Ω is reaction zone sensor, and
σ_t is the turbulent Prandtl number.

The thickening factor is calculated as

$$F = 1 + (F_{max}^{loc} - 1)\Omega \tag{2.22}$$

where F_{max}^{loc} is the maximum flame thickening factor at each local cell, this is calculated as

$$F_{max}^{loc} = min(F_{max}, N \times \frac{\Delta}{\delta_L}) \tag{2.23}$$

where

F_{max} is the maximum flame stretch factor,
N is the number of cells in the flame, and
Δ is the cell size.

2.7.2 Flamelet Model

A flamelet model is designed to reduce computational costs in simulations by precomputing reactions for representative scenarios and tabulating them for relevant quantities. It assumes

that the flame is thin which leads to turbulence being unable to affect the inner structures [27]. When this occurs, the thermo-chemistry is no longer coupled with turbulence as it normally is in combustion. The flame can thus be seen as a collection of laminar flamelets. These flamelets are calculated by parameterizing the temperature and species within the flame by two or more variables. In flamelets, the reaction progress variable c signifies the chemical state within a cell, indicating unburnt conditions ($c = 0$), burnt conditions ($c = 1$), or any intermediate state ($0 < c < 1$). As previously mentioned, this study uses the FGM model, which parameterizes mixture fraction, enthalpy, and reaction progress variable, which is initially unnormalized and defined as

$$y = \sum_k (MW_k Y_k) \tag{2.24}$$

where

MW_k is the molar weight of species k, and
Y_k is the mass fraction.

The y transport equation can be formulated as

$$\frac{\partial \rho y}{\partial t} + \nabla \cdot (\rho \mathbf{v} y) = \nabla \cdot (\Gamma_y \nabla y) + \dot{\omega}_y \tag{2.25}$$

where

Γ_y is the diffusivity of the progress variable, and
$\dot{\omega}_y$ is the source term.

Finally, the progress variable can then be computed as [28]

$$c = \frac{y - y_u}{y_b - y_u} \tag{2.26}$$

where

y_u is the unnormalized progress variable at the initial unburnt state, and
y_b is the unnormalized progress variable at the burnt state.

There are several options for calculating the source term of the progress variable, $\dot{\omega}_y$. In this study, two methods are presented—Kinetic Rate (FGM Kinetic) and Turbulent Flame Speed Closure (TFC). For the former option, the source term is derived from the chemical kinetic reaction rate, which is interpolated from a flamelet table. For the latter option, the source term is calculated from the following flame propagation method [29]

$$\dot{\omega}_{y,tfc} = \rho_u S_t |\nabla y_{mean}| \tag{2.27}$$

where

ρ_u is the density of the unburnt mixture,
S_t is the turbulent flame speed, and
y_{mean} is the time-averaged progress variable.

There are several methods for calculating the turbulent flame speed, S_t, one of which is proposed by Zimont *et al.* [29], as the following expression

$$S_t = 0.5G(u')^{3/4} S_L^{1/2} \alpha_u^{-1/4} L_T^{1/4} \tag{2.28}$$

where

G is the stretch factor,
u' is the turbulent velocity,
α_u is the thermal diffusivity of the unburnt mixture, and
L_T is the integral length scale.

For further information, refer to [29].

Finally, there are different methods for computing flamelet tables, named reactor types. Two different types of reactors have been included in this study—0D Ignition and 1D Premixed Freely Propagating (PFP). The former is similar to auto-ignition where only the time dimension is considered, the following equations are solved for each mixture fraction and heat loss ratio in the tabulation process [30]

$$\begin{aligned} \frac{\partial Y_i}{\partial t} &= R_{i,kin} \\ \frac{\partial T}{\partial t} &= \sum_{i=1}^{N} \frac{h_i R_{i,kin}}{C_p} \end{aligned} \tag{2.29}$$

where

$R_{i,kin}$ is the chemical kinetic reaction rate for species i,
h_i is the specific enthalpy, and
C_p is the specific heat capacity.

The 1D PFP equations are more substantial and are elaborated on in [30] but are not outlined here. The equations are constructed in physical space by a spatial coordinate and then transformed into progress variable space. They are then solved by setting boundary conditions for the unburnt and burnt sides for the progress variable, temperature, and species mass fractions. By solving these equations the laminar flame speed is tabulated for a specific range of conditions that can later be used in the simulations.

2.8 Fuel Chemistry

A2, or Jet A, is a kerosene-based fuel comprising various hydrocarbons, including n-paraffins, iso-paraffins, cycloparrafins, and aromatics. These hydrocarbons exhibit a wide range of carbon numbers, spanning from 8 to 18 [31]. In contrast, the SAF C1 predominantly contains iso-paraffins with only carbon numbers 12 and 16 present, with the latter being present in a smaller amount. Additionally, C1 contains only about 1% aromatics, whereas A2 has a significantly higher aromatic content of 17% by volume. The aromatic content of fuel is

important for the practical use of a fuel. The aromatics help the gaskets in the fuel system to swell by chemical reactions, thereby reducing the likelihood of leakage, a critical concern, especially in aviation. Due to its low aromatic content and other factors, C1 is only accepted in the aviation industry when blended with A2, with C1 comprising no more than 50% of the mixture [31].

Something closely related to fuel chemistry and essential for CFD is the reaction mechanisms of the fuels being combusted. These reaction mechanisms, discussed in Section 2.5.2, detail the pathways of chemical reactions occurring when the fuel is combusted [32]. For jet fuels, there are two families of skeletal reaction mechanisms—ZXX [11] and HyChem (Hybrid Chemistry) [8] [9] [10]. One of the main assumptions when utilizing a skeletal reaction mechanism is that the fuel usually is modeled as a single type of hydrocarbon molecule. The wide range of carbon numbers in A2 can render it inaccurately represented as a single hydrocarbon molecule. The model formulas for A2 and C1 are presented in Table 3.6, with further discussion provided in Section 3.5.

2.9 NO_x Formation

The term NO_x is used to group nitric oxides NO and NO_2. During combustion, they can be produced at varying concentrations but NO is the dominating species [33]. The formation of NO_x in combustion is usually divided into three types of formations, Thermal, Prompt, and Fuel.

Thermal NO_x formation occurs when nitrogen in the air reacts with oxygen due to elevated temperatures. To model this formation the Zeldovich mechanism [34] has three reversible reactions that are implemented to take NO_x formation into consideration. These three reactions are given as [34]

$$N_2 + O \iff NO + N \tag{2.30a}$$
$$N + O_2 \iff NO + O \tag{2.30b}$$
$$N + OH \iff NO + H \tag{2.30c}$$

In the same order as the reactions in 2.30, the reaction rate coefficients are given in unit $m^3/(kmol{\cdot}s)$ as [34]

$$k_1 = 1.8 \times 10^{11} e^{-\left(\frac{38370}{T}\right)} \tag{2.31a}$$
$$k_2 = 1.8 \times 10^{7} T e^{-\left(\frac{4680}{T}\right)} \tag{2.31b}$$
$$k_3 = 7.1 \times 10^{10} e^{-\left(\frac{450}{T}\right)} \tag{2.31c}$$

The Zeldovich reactions only contribute to NO_x formations at elevated temperatures due to the high amount of energy required to break the strong triple bond of the N_2 molecule, which can be seen in the high activation energy in equation 2.31a. The reactions are completely dependent on k_1 being sufficiently; without elevated temperatures, these reactions will not produce NO_x.

The second type, Prompt NO_x is the formation of NO_x by way of intermediary species such as CH, CH_2, HCN, CN. To model this in detail, several complex reactions are needed. To simplify this, De Soete [35] proposed a global reaction accounting for the most important pathways. Using a production rate of Prompt NO_x formation given as

$$\dot{\omega}_{NO_x,prompt} = k_r MW_{NO_x} \tag{2.32}$$

where MW_{NO_x} is the molar weight of NO_x, and k_r is the reaction rate constant given by

$$k_r = cf(F)A[O_2]^a[N_2][Fuel]e^{-(\frac{E_a}{R_u T})} \tag{2.33}$$

where

cf is a correction factor,
F is a factor computed for a given fuel,
A is a pre-exponential factor, and
a is an exponent that varies with the oxygen mole fraction.

The pre-exponential factor *A* is computed by

$$A = 10^6(\frac{R_u T}{p})^{(a+1)} \tag{2.34}$$

The last type is Fuel NO_x which is applicable if the fuel contains nitrogen, and is therefore not included in this study. For further information refer to [34] for the Thermal NO_x, and [35] for the Prompt NO_x.

2.10 Thermal Radiation

In combustion processes, radiation is emitted by high-temperature atoms in the combustion zone as a result of the chemical reactions producing heat. Heated surfaces will emit, reflect, and transmit radiation, while the participating media between surfaces will absorb, emit, or scatter radiation. The amount of radiation each surface receives or emits will depend on this. The radiative transfer equation (RTE) governs the process of radiation traveling through a medium, the intervening material absorbs and increments its radiant intensity, *I*, in the Ω direction. This equation can be written in terms of radiant intensity for a specific wavelength, λ, as the following [36]

$$\frac{dI_\lambda}{ds} = -\beta_\lambda I_\lambda + k_{a\lambda} I_{b\lambda} + \frac{k_{s\lambda}}{4\pi}\int_{4\pi} I_\lambda \Omega d\Omega + \frac{k_{ps\lambda}}{4\pi}\int_{4\pi} I_\lambda \Omega d\Omega \tag{2.35}$$

where

I_λ is the radiative intensity at wavelength λ,
$I_{b\lambda}$ is the black body intensity at λ,
s is the distance in the Ω direction,
β_λ is the extinction coefficient, and
Ω is the solid angle.

The extinction coefficient β_λ is defined as [36]

$$\beta_\lambda = k_{a\lambda} + k_{s\lambda} + k_{pa\lambda} + k_{ps\lambda} \tag{2.36}$$

where

$k_{a\lambda}$ is the absorption coefficient at λ,
$k_{s\lambda}$ is the scattering coefficient at λ,
$k_{pa\lambda}$ is the particle absorption coefficient at λ, and
$k_{ps\lambda}$ is the particle scattering coefficient at λ.

The method of spherical harmonics transforms the RTE stated in equation 2.35 into a group of partial differential equations within 3D space. It achieves this by converting the continuous directional variation of radiative intensity into a sequence of orthogonal functions termed spherical harmonics [36]. These harmonics effectively simulate the anisotropic propagation of thermal radiation, with the directional patterns expressed through spherical harmonic functions.

The radiative intensity field, $\mathbf{I}(\mathbf{r}, \hat{\mathbf{s}})^3$, at a specific point $\mathbf{r}$ within the medium can be seen as a value of a scalar function on the surface of a sphere with a unit radius enclosing the point $\mathbf{r}$. Any such function can be represented using a two-dimensional generalized Fourier series [36]

$$\mathbf{I}\left(\mathbf{r}, \hat{\mathbf{s}}\right) = \sum_{l=0}^{\infty} \sum_{m=-l}^{l} I_l^m\left(\mathbf{r}\right) \Upsilon_l^m\left(\hat{\mathbf{s}}\right) \tag{2.37}$$

where

$\hat{\mathbf{s}}$ is the direction unit vector,
$I_l^m(\mathbf{r})$ are position-dependent intensity coefficients, and
$\Upsilon_l^m(\hat{\mathbf{s}})$ are the spherical harmonics.

When the series in equation 2.37 is truncated to $l = [0, 1]$, the spherical harmonics reduce to their lowest order, known as the P1 model, represented by the following equation [36]

$$I\left(\mathbf{r}, \hat{\mathbf{s}}\right) = I_0^0\Upsilon_0^0 + I_1^{-1}\Upsilon_1^{-1} + I_1^0\Upsilon_1^0 + I_1^1\Upsilon_1^1 \tag{2.38}$$

After several assumptions and equation manipulations, the P1 model can be presented by the following equations according to Modest [36]

$$\begin{cases} \nabla \cdot \mathbf{q} = k(4\pi I_b - G) & \text{(2.39a)} \\ \nabla G = -(3\beta - A_1\sigma_s)\mathbf{q} & \text{(2.39b)} \end{cases}$$

where

$\mathbf{q}$ is the radiative heat flux,
G is the incident radiation
A_1 is the scattering factor, and
σ_s is the scattering coefficient.

The divergence of the radiative heat flux, $\nabla \cdot \mathbf{q}$, in equation 2.39a will then be added as a source term in the NSE energy equation 2.3.

To consider the effect of a medium containing absorbing and emitting molecules, one can employ the Full Spectrum Correlated-k Distribution (FSCK) model. Research by Modest and Zhang [37] demonstrated that the Weighted Sum of Grey Gases (WSGG) model is only a crude implementation of the FSCK model. The FSCK model can be integrated with various solution models to address the RTE, in this case, the P1 model. For further information about the FSCK refer to [37].

2.11 PLIF Imaging

2D fluorescence imaging was initially demonstrated in the early eighties [38]. Investigations and applications rapidly followed in various fields such as combustion research, fluid dynamics, and environmental science. It later came to be called Planar Laser-Induced Fluorescence (PLIF). The method involves using a high-energy pulsed UV together with a dye laser to adjust the wavelength light to excite molecules, thus causing them to fluoresce, which means that they re-emit light. This is done to enable visualization of the target species concentration in a 2D plane. This can be done for all sorts of molecules and species, specifically for OH and CH_2O, which has been used in the benchmark of this study [7]. The PLIF signal is proportional to the amount of molecules that fluoresce. Something important to keep in mind is that the laser intensity is the highest in the centerline of the laser beam. Further away from the centerline the intensity decreases, causing the fluorescence of the molecules in the area to be lower and thus causing the visualization of the species concentration to be less clear [38]. This can affect the imaging by giving less accurate results in regions further away from the centerline.

3 Implementation

This chapter describes how the work has been carried out, what sensitivity studies have been performed, and what settings and boundary conditions have been used for the models in the CFD software. The work of this study was initiated with several 2D RANS cases to get a better understanding of the software STAR-CCM+ (v2310r8) and its models. Consequently, all simulations in 2D RANS in Section 3.3 are conducted using fuel A2 only. Fuel C1 is reserved for the subsequent 3D LES simulations where a validation study is performed against the benchmark experiment [7]. The implementation of this validation study is presented in Section 3.4.

3.1 Discretization Schemes

This section provides a brief overview of the discretization scheme settings utilized in the software, most of which are default. For the segregated flow solver, a bounded central differencing scheme is used. The upwind blending factor specifies the proportion of upwind differencing and is set to the default value 0.15. The convection term for segregated fluid enthalpy and species are set to 2nd order upwind scheme, with secondary gradients enabled. Finally, the limiter method used for gradients is Venkatakrishnan [39] and the algorithm used for time advancement was Pressure-Implicit with Splitting of Operators, PISO [14]. The number of correctors was around 3 throughout all simulations. The residual reduction was set to 0.25, and the time-step for LES was set to 5e-6 to keep the average CFL number below 1.

3.2 Initial & Boundary Conditions

It is assumed that the domain is initially full of ambient air moving at a speed of 1 m/s in the axial direction. Important to mention is also that air is assumed to consist of mass fractions of 0.233 O_2 and 0.767 N_2. The conditions are presented in Table 3.1.

Table 3.1: Initial conditions.

u [m/s]	Y [-]	p [atm]	T [K]
1	O_2: 0.233 N_2: 0.767	1	293

The boundaries that have been specified with certain conditions are the inlet for fuel (mixture) and co-flow inlet for air (surrounding), the outlet, the walls, and for the 2D case also the symmetry axis. The boundaries are illustrated in Figure 3.1, and the boundary conditions (BC) for the 2D and 3D cases are presented in Table 3.2. The main difference in BCs

between 2D RANS and 3D LES is the symmetry axis which is only present in 2D, as it helps to reduce computational costs.

Table 3.2: Boundary conditions.

	u [m/s]	**Y [-]**	**p [atm]**	**T [K]**	**I [%]**	**L [m]**
Inlet Air	1	O_2: 0.233 N_2: 0.767	ZG	293	-	-
Inlet Fuel A2	13.829	O_2: 0.2207 N_2: 0.7264 Fuel: 0.0529	ZG	393	20	0.0024
Inlet Fuel C1	13.829	O_2: 0.2204 N_2: 0.7256 Fuel: 0.0540	ZG	393	20	0.0024
Outlet	ZG	ZG	1	ZG	-	-
Walls	No-slip	ZG	ZG	Adiabatic	-	-
Symmetry (2D)	ZG	ZG	ZG	ZG	-	-

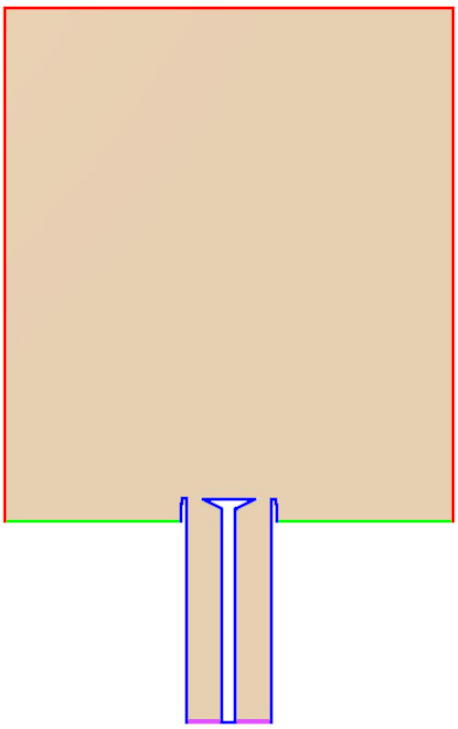

Figure 3.1: Boundaries in the XY-plane of the domain. Magenta for inlet fuel, green for inlet air, red for outlet, and blue for walls.

The inlet velocity for the fuel was computed from Pathania *et al.* [7] by setting the bulk velocity, U_b, at the bluff-body to 23.5 m/s. The mass fractions for the fuels are calculated with far-from-blow-off conditions, where ϕ/ϕ_{bo} = 1.2. It is important to note that the close-to-blow-off conditions, where ϕ/ϕ_{bo} = 1.01, are not included in this study. The turbulence intensity (I) and turbulence length scale (L) were inherited from the RANS case, and directly implemented into the LES case. Using the same conditions for the turbulence

in LES as in RANS resulted in somewhat lower downstream turbulence intensity, and also introduced pressure oscillations in the annular pipe caused by resonance. To address this issue, a mass flow scaling boundary condition was implemented, complementing the synthetic turbulence model. This approach maintains a constant mass flow of air-fuel mixture, while allowing velocity fluctuations to occur and proved capable of reducing the pressure oscillations sufficiently.

3.3 2D RANS

This section presents the implementations specific to the 2D RANS case, utilizing a steady-state solver. A mesh sensitivity study has been performed along with a turbulence sensitivity study.

3.3.1 Mesh Sensitivity Study

To optimize the mesh and find a balance between accuracy and computational time, a simple mesh sensitivity study was initially performed in 2D RANS. Three meshes of different fineness were designed, and their information is given in Table 3.3.

Table 3.3: RANS Mesh sensitivity study.

	Mesh A	**Mesh B**	**Mesh C**
Number of cells	$\sim$125K	$\sim$185K	$\sim$335K
Min cell size [mm]	$\sim$0.25	$\sim$0.2	$\sim$0.15

The combustion model used for the sensitivity study is FGM with Kinetic Rate (FGM Kinetic) to calculate the source term of the progress variable, using the 0D reactor type, with reaction mechanism Z79 for fuel A2. The reason why this specific model was used is solely because it should have a low computational cost compared to FRC models. The OH and CH_2O concentration results, calculated as normalized number densities, are presented in the mesh sensitivity study shown in Figure 3.2.

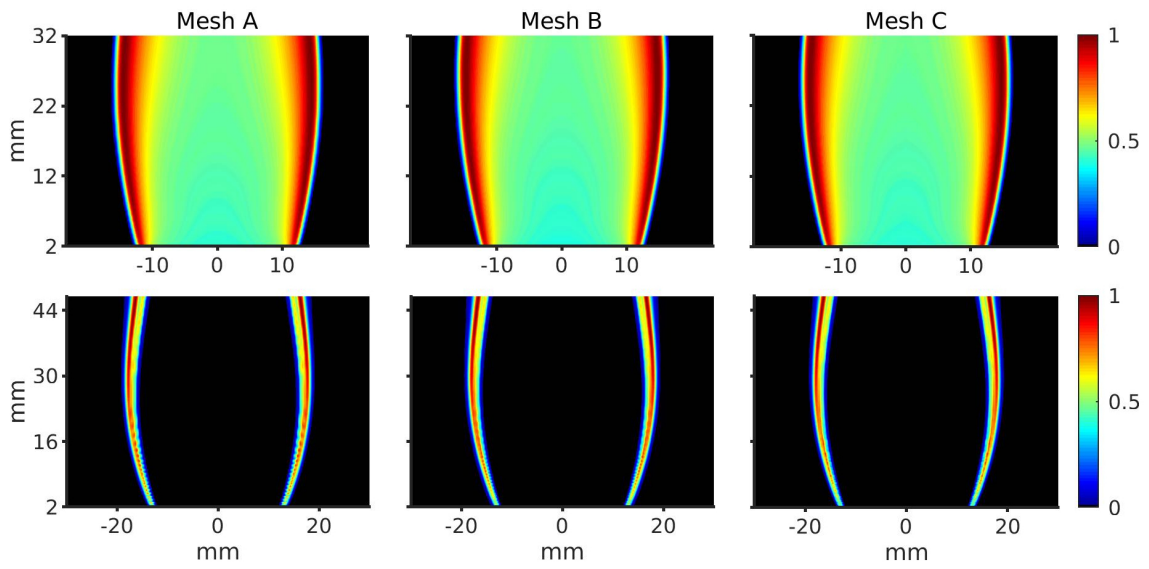

Figure 3.2: RANS Mesh sensitivity study. The first row presents results for OH and the second row presents results for CH_2O.

As there were no significant differences in results, the decision was made to proceed with the coarsest mesh, Mesh A, as it appeared to be sufficient.

3.3.2 Turbulence Sensitivity Study

Pathania *et al.* [7] show that the turbulence intensity at the bluff-body is 20%. A turbulence sensitivity study was performed to try to match the benchmark result [7] by using different turbulence intensities as boundary conditions for the inlet of the annular pipe. The results are presented in Table 3.4.

Table 3.4: Turbulence intensity study for the RANS case.

Intensity BC at inlet [%)]	**Intensity at bluff-body [%]**
5	7.0
12.5	9.1
20	10.3

The turbulence intensity at the bluff-body appears to increase initially with an increase in the inlet boundary condition. However, when further increasing the BC intensity, the increase tapers off nonlinearly at the bluff-body. Qualitative images indicate that there is turbulent flow in the pipe, and further increases in turbulence intensity BCs are unlikely to notably increase turbulence intensity downstream. Therefore it was deemed sufficient to choose a BC of 20%, resulting in a turbulence intensity of 10.3% at the bluff-body. Fully developed flow is assumed, accompanied by small turbulent eddies along the boundary layer of the walls. The turbulence length scale of these eddies is estimated to be around 7% of the pipe diameter, and this is prescribed as a boundary condition at the inlet. It is important to note that a longer length scale is likely to lead to more persistent turbulence downstream because of the turbulent energy cascade. However, this will be further discussed in Section 5.2.

3.4 3D LES

The implementations specific to the 3D LES case are presented in this section. A mesh sensitivity study has been performed. The data for the LES cases were extracted over 50 milliseconds with 20 snapshots per millisecond. The scalars that were extracted included density, temperature, pressure, velocity, OH, CH_2O, and NO_x mass fractions.

3.4.1 Mesh Sensitivity Study

A brief sensitivity study for the 3D LES case was also conducted using FGM A2 Z79, where two meshes were compared, see Figure 3.3, where (a) is the coarse mesh and (b) is the fine mesh. The two meshes were created in STAR-CCM+ using a structured, trimmed mesher with predominantly hexahedral elements. Several regions were defined with varying refinements and hanging nodes in between regions. No prism layers were added to resolve the boundary layers, instead a wall function was used. The whole domain is meshed, using no symmetry assumptions for the 3D LES case. The pipe section preceding the bluff-body extends for a length equal to $4 \times D_{bb}$, where D_{bb} is the bluff-body diameter, which aids in the flow development. The radius and the length of the domain after the bluff-body are set to $4 \times D_{bb}$ and $8.5 \times D_{bb}$, respectively.

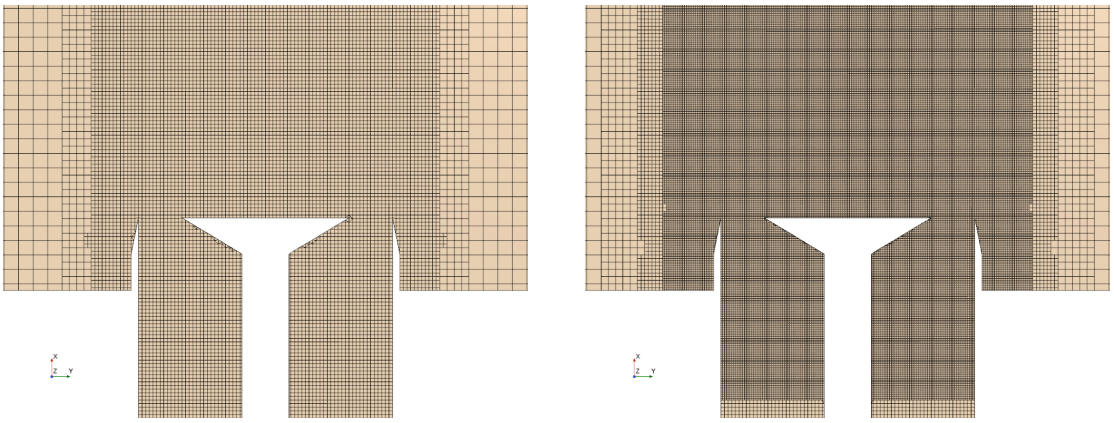

(a) **(b)**

Figure 3.3: Two LES mesh configurations (a) Mesh 1 and (b) Mesh 2.

The details of the meshes are presented in Table 3.5.

Table 3.5: LES Mesh properties.

	Mesh 1	**Mesh 2**
Number of cells	$\sim$ 4M	$\sim$ 16M
Min cell size [mm]	$\sim$ 0.5	$\sim$ 0.25

Generally, the meshes have been designed to cover the annular pipe and bluff-body with smaller cells as well as have a large enough diameter in the domain to be able to capture the shear layers. When the mesh goes from the fine region to the coarse region, a transition

region has been implemented to avoid a drastic change in cell size and risk affecting the results. The results from the mesh sensitivity study are presented in Figure 3.4, where the Thickened Flame Model has been used for fuel A2.

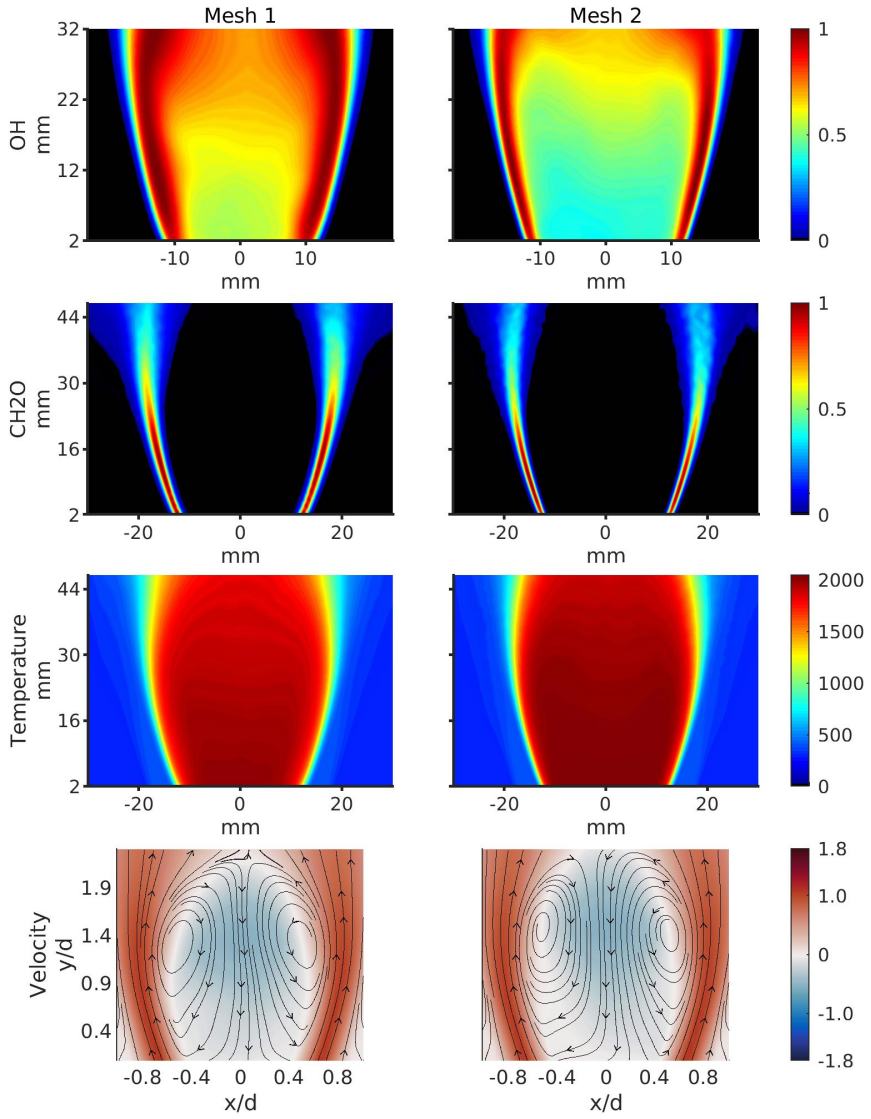

Figure 3.4: Mesh sensitivity study for LES. Rows present time-averaged OH concentration, CH_2O concentration, temperature, and axial velocity, respectively.

The results from the sensitivity study show notable differences in all four quantities. The coarse mesh with the TF model seems to incorrectly smear the results due to low resolution coupled with the high diffusion of the model. At this stage, a third and more detailed mesh should have been introduced, however, Åkerblom *et al.* [40] utilized Partially Stirred Reactor (PaSR) to determine that $\sim$16M cells and a minimum cell size of $\sim$0.25 mm were outside of the mesh sensitivity region. It is not the same model as used in this study but the mesh sensitivity results are deemed sufficient since the difference between M1 and M2 is acceptably small.

3.5 Reaction Mechanisms

Reaction mechanisms were introduced in Section 2.5.2, and for the 2D RANS case, two different types have been implemented—Z79 and HyChem skeletal. Their general information is given in Table 3.6.

Table 3.6: Reaction mechanism information.

	Z79 A2	**Z79 C1**	**HyChem A2**	**HyChem C1**
Model formula	$C_{11}H_{22}$	$C_{13}H_{28}$	$C_{11}H_{22}$	$C_{13}H_{28}$
Number of species	31	31	41	42
Number of reactions	79	79	202	286

3.5.1 Z79

The Z79 reaction mechanism is part of a series of mechanisms that can be referred to as ZXX, with each specific mechanism named according to the number of reactions it includes. They are developed by Zettervall [11] to facilitate detailed simulations in 3D LES, where larger reaction mechanisms are too costly. It is available for both fuels, A2 and C1, with general details provided in Table 3.6. In Zettervall [11] it was demonstrated that the Z79 mechanism exhibits good agreement with experimental data for parameters such as laminar flame speed and ignition delay time. Notably, it also captures Negative Temperature Coefficient (NTC) behavior, wherein the ignition delay time is relatively short for low temperatures, which is otherwise difficult for reduced mechanisms to predict. For this study, the Z79 mechanism was employed in both 2D RANS and 3D LES.

3.5.2 HyChem Skeletal

Stanford University has a whole collection of reaction mechanisms with the name HyChem (Hybrid Chemistry) [8] [9] [10]. They range from the least detailed mechanisms which they call ”skeletal” or ”reduced” to the more advanced which they simply call ”detailed”. The reaction mechanism that is used in this study is the skeletal. There are separate mechanisms for A2 and C1, and their general information can be found in Table 3.6. The reason why these specific reaction mechanisms were used is because they simply give enough information for the case while keeping computational costs in consideration [19]. It was only used for RANS but not for LES, unlike Z79, and the reasoning for this is discussed in Section 5.1.

3.6 Combustion Models

As outlined briefly in Section 2.7, this study will investigate a set of turbulence-chemistry models, referred to as combustion models in STAR-CCM+, which further divides them into two categories—reacting species transport models and flamelet models, where the former can be likened to Finite Rate Chemistry. Among them are three reacting species transport

models—LFC, EDC, and TFM—alongside one flamelet model, FGM. In the RANS study LFC, EDC, and FGM will be included. FGM is used with both TFC and Kinetic Rate, but as the results for the former are poor, most likely due to incorrect implementation, they are not presented. Further explanation of TFC and Kinetic Rate is presented in Section 2.7.2. For the LES study, EDC, and TFM will instead be included, alongside FGM TFC which in the LES case is simply referred to as FGM.

Keep in mind that all equations and model implementation in the following section are taken from STAR-CCM+ documentation, and as such have no citation.

3.6.1 LFC & EDC

In STAR-CCM+, Complex Chemistry is a collection of combustion models within the reacting species transport family, which can be likened to the theoretical FRC model and includes LFC and EDC models. In Complex Chemistry, during each time-step, the model integrates the chemical state in each cell over a certain time, called the chemical time-step. This is performed using a stiff ODE solver on the equation given as

$$Y_i^\tau = Y_i + \int_0^\tau q_j(\mathbf{Y}, T, p)\, dt \tag{3.1}$$

where

Y_i^τ is the mass fraction of species i at the end of time integration,
Y_i is the mass fraction of species i,
q_j is the rate of progress of a specific reaction *j*,
Y is the mass fraction vector, and
τ is a time scale depending on the turbulence-chemistry model.

The explicit reaction source term for species i is given as

$$\dot{\omega}_i = \rho f \frac{(Y_i^\tau - Y_i)}{\tau} \tag{3.2}$$

where f is the scaling factor.

The first model Complex Chemistry model, Laminar Flame Concept, utilizes τ in equation 3.2 to denote the time-step in transient simulations, while for steady simulations, τ represents the residence time, $\frac{\dot{m}}{m}$. The scaling factor, *f*, in equation 3.2 is set to unity for LFC. This is because LFC assumes a quasi-laminar flame and therefore does not include any scaling of the reaction source term.

The second Complex Chemistry model examined in this study is the Eddy Dissipation Concept, which in STAR-CCM+ is implemented according to Magnussen [22]. By extending the FRC model, EDC accounts for the turbulence-chemistry interaction through a scaling factor determined by the following expression

$$f = \left(\left[C_l \left(\frac{\nu \tau_{turb}}{L^2} \right)^{0.25} \right]^{-3} - 1 \right)^{-1} \tag{3.3}$$

where

C_l is the fine structure length constant, 2.1377,
ν is the kinematic viscosity, and
τ_{turb} is the turbulent time scale.

The turbulent time scale, τ_{turb}, is calculated as a constant, 0.4082, times the Kolmogorov time scale, $\sqrt{\frac{\nu}{\varepsilon}}$. The time scale τ in equation 3.2 is set to τ_{turb} in this model.

As previously mentioned, the EDC implementation in STAR-CCM+ follows Magnussen [22] which is appropriate for RANS but might prove erroneous for LES. Studies such as Panjwani *et al.* [25] suggest that the basic EDC model uses a model constant based on RANS and does not account for the fine structure region. There is a solution to this issue where the fine structures are properly taken into account. However, it is not effectively implemented in the software, causing the EDC model to exhibit LFC behavior in LES, as discussed in Section 5.2. An additional model that did not assume a quasi-laminar flame was therefore needed in the LES study and after deliberations with the supervisor the Thickened Flame Model was deemed appropriate.

3.6.2 Thickened Flame Model

This model is implemented in STAR-CCM+ in a similar way as presented in Section 2.7.1.3, by artificially increasing the flame thickness to enable the flame to be resolved on the mesh. This model is therefore only available for LES. Some further choices have to be made to use the model in the software. For the reaction zone sensor, reaction rate has been used, and for efficiency function, the Power-Law model. Finally, for laminar flame thickness, the Sutherland Law of Thermal Diffusivity has been used. For further information, refer to Durand and Polifke [26].

3.6.3 Flamelet Generated Manifold

In STAR-CCM+, the Flamelet Generated Manifold model specifically assumes that the thermochemical conditions within the turbulent flames are similar to those in the laminar flames. It is done by parameterizing the reaction progress variable, mixture fraction, and enthalpy. This results in only one chemical time scale—the one of the heat release reactions. When deciding which species to include in the FGM table, it is of importance to only include those that require tabulation, however, the sum of the mass fractions should be close to 1. Opting for only the essential species for post-processing purposes will improve tabulation time. The tabulated species are Fuel (A2: $C_{11}H_{22}$ and C1: $C_{13}H_{28}$), CH_2O, CO, CO_2, H, H_2, H_2O, N_2, O, O_2, OH. The unnormalized progress variable in equation 2.26 is calculated using CO and CO_2, since they are commonly found products in the combustion process.

There are a few alternatives for calculating the progress variable source term, $\dot{\omega}_y$, in the species transport equation 2.5. As previously mentioned, in this study the Kinetic Rate and Turbulent Flame Speed Closure are included. These are presented in Section 2.7.2. In RANS, both methods were tested. However, the TFC method failed to yield accurate turbulent flame speed values, resulting in a nonphysical flame expansion. This discrepancy was

likely due to poor implementation, either within the software or in the case setup. Therefore, TFC results are not presented at all, for RANS. In LES, both methods were also tested, and TFC proved more appropriate in this case. This explains why Kinetic Rate is used in RANS while TFC is used in LES. Both 0D Ignition and 1D PFP were assessed in RANS, whereas only 1D PFP was employed in LES. The choice of 1D PFP stemmed from its theoretical suitability to this case because of several factors, such as the inclusion of laminar flame speed. The simulation case is a flame propagating from a burnt region of products towards an unburnt region of reactants, this is in itself similar to the equations that 1D PFP solves during tabulation. 0D Ignition, however, assumes auto-ignition where the only dimension is time, which is not fitting for this case but would be better suited to for instance an internal combustion case.

3.7 NO_x Emission Model

When the NO_x emission model is chosen in STAR-CCM+, three optional NO_x models can be added; NO_x Thermal, Prompt, and Fuel. These models are implemented in the software in the same way as presented in Section 2.9. In this study, only NO_x Thermal and Prompt are used, since both fuels only contain hydrocarbons, and therefore do not apply to the NO_x Fuel model. Once NO_x Thermal and Prompt values are computed, they are summed and in STAR-CCM+ denoted as NO_x emissions.

3.8 Thermal Radiation

When implementing radiation in the software the P1 model is used, which in STAR-CCM+ is denoted as Participating Media Radiation (Spherical Harmonics). The radiation spectrum option chosen for the model is k-Distribution Thermal Radiation, which only takes the effects of the most common combustion products CO_2 and H_2O into account. Default values of 8 quadrature points and a Gauss quadrature shape factor of 1.5 are chosen for the model, as the software documentation recommends it for most cases. The radiation temperature chosen for the thermal environments is 293 K which is the ambient temperature of the domain.

4 Experimental Benchmark

The results from the experiments performed by Pathania *et al.* [7] can be seen in Figures 4.1-4.3. The analysis of the instantaneous results in Figure 4.1 revealed elevated concentrations of OH within the shear layer, contrasted by lower levels within the recirculation zone. In the flame fronts close to the bluff-body, Kelvin-Helmholtz instabilities were observed, which contributed to the wrinkling of the flame.

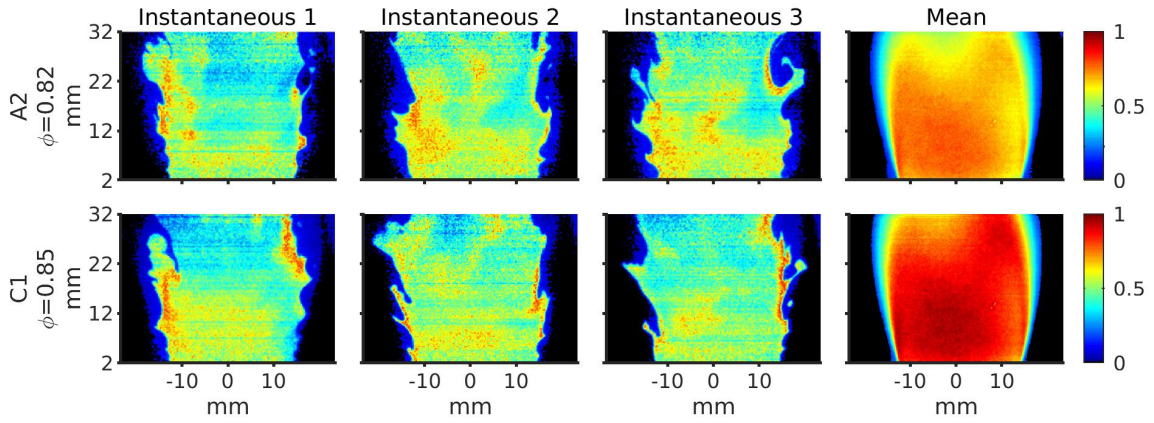

Figure 4.1: Instantaneous (column 1-3) and average (column 4) OH-PLIF images with A2 and C1 reproduced from Pathania *et al.* [7].

It is important to note that the OH mean plot for A2, although not visible, has an error, revealed as a thin and uniform red line below the X-axis. This line causes a colormap error, thus explaining why A2 appears so different from C1, regarding OH mean.

The OH-PLIF images were further analyzed to obtain statistical results, such as the time-averaged progress variable which is then used for deciding the location of data points in Figure 5.7.

The instantaneous CH_2O results in Figure 4.2 reveal a notable concentration along the shear layer, occasionally accompanied by rather fine vortex-like structures. Correspondingly, the mean of the instantaneous results (column 4) portrays a similar structure.

In Figure 4.3, the normalized mean axial velocity, $\langle u \rangle / U_b$, is presented for both unreacting flow (left) and reacting flow (right). These results were obtained using Particle Image Velocimetry (PIV) [7]. The reacting flow plot is extracted from a heptane flame, which constitutes the only velocity result provided by Pathania *et al.* [7] that is pertinent to this study. It is sufficiently comparable with A2 and C1 results and is therefore chosen to be included for validation purposes. It is worth noting that there is a colormap issue in Figure 4.3. The magenta line is meant to represent the recirculation zone, which matches well with the streamlines but not with the color plot.

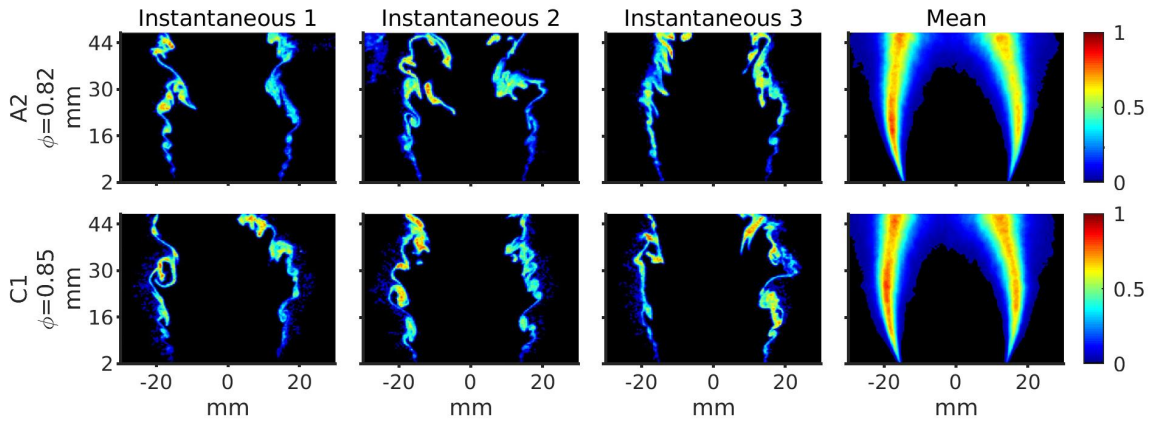

Figure 4.2: Instantaneous (column 1-3) and average (column 4) CH_2O-PLIF images with A2 and C1 reproduced from Pathania *et al.* [7].

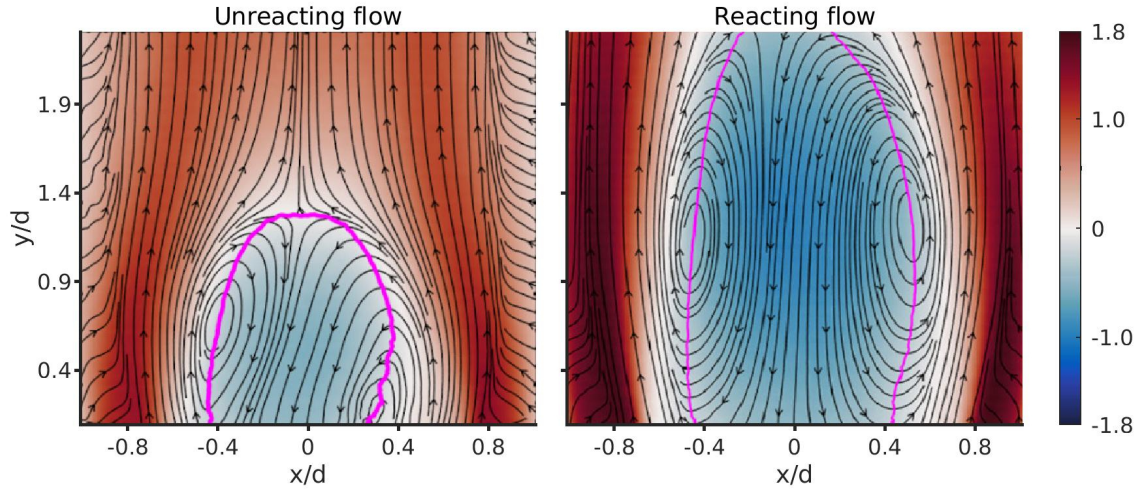

Figure 4.3: Normalized mean axial velocity $\langle u \rangle / U_b$ for unreacting flow (left) and reacting flow (right) reproduced from Pathania *et al.* [7].

These velocity results along with a few others presented by Pathania *et al.* [7], are used for producing further results such as a Borghi diagram and a turbulence intensity diagram. These results, together with simulation results, are presented in Section 5.2.

5 Results & Discussion

Initially, the RANS results are presented to gain insight into the combustion models and reaction mechanisms. The results for OH and CH_2O are calculated as number density indicating the total number of molecules per unit volume. The results are normalized to get a concentration ranging from 0 to 1. Subsequently, the validation study in LES is presented and compared to the benchmark results in Section 4. Finally, the NO_x emission results and radiation effects are presented. NO_x is calculated as a mass fraction and is not normalized, unlike the previously explained quantities.

5.1 RANS

The results for the 2D RANS simulations are presented in Figures 5.1-5.3. When comparing OH in Figure 5.1 it can be surmised that it is more spread out in the recirculation zone when using Z79 mechanisms. For HyChem, the OH is more concentrated near the flame fronts.

The EDC model can be considered to yield the best agreement with the benchmark results in Figure 4.1 since OH is more spread out in the recirculation zone compared to the other combustion models. Furthermore, the diameter of the flame seems to decrease in the axial direction which is consistent with experiments. All four models seem to produce too wide flames, or flame diameters. It can be seen in Figure 4.3 that the recirculation zone increases significantly in size for the reacting flow compared to the unreacting flow. This is caused by the volumetric expansion of the combustion, thus a stronger flame might be the reason for the large flame diameter. The EDC model for instance has a weaker flame, or more precisely, a slower reaction rate than LFC as discussed in Section 2.7.1, which is indicated by a smaller flame diameter and a broader high-concentration OH layer.

The FGM model with the use of Kinetic Rate and 1D PFP (FGM Kinetic 1D) seems to give quite similar results as the LFC model. The reason for this might be that the diffusion in the progress variable transport equation is too strong for FGM Kinetic leading to a higher consumption rate. The FGM model with the use of Kinetic Rate and 0D Ignition (FGM Kinetic 0D) does not have the same behavior, which can be explained by the assumption of homogeneous mixture and auto-ignition during the tabulation. Therefore, no spatial gradients nor temperature and mixture fraction profiles are present, and this can potentially result in slow reaction rates. This in turn can counteract the high diffusion, resulting in a slower consumption speed and a smaller diameter of the flame compared to the FGM Kinetic 1D.

The FGM Kinetic 0D and EDC are quite similar, not regarding the OH distribution but rather the flame diameter. The reason for this might be that the reaction rates are slower. For EDC this can be explained by the reduction factor from equation 3.3 that reduces the reaction source term leading to a slower reaction rate. For FGM Kinetic 0D, this is not as easily explained. It relates to the assumptions made during tabulation, as previously stated.

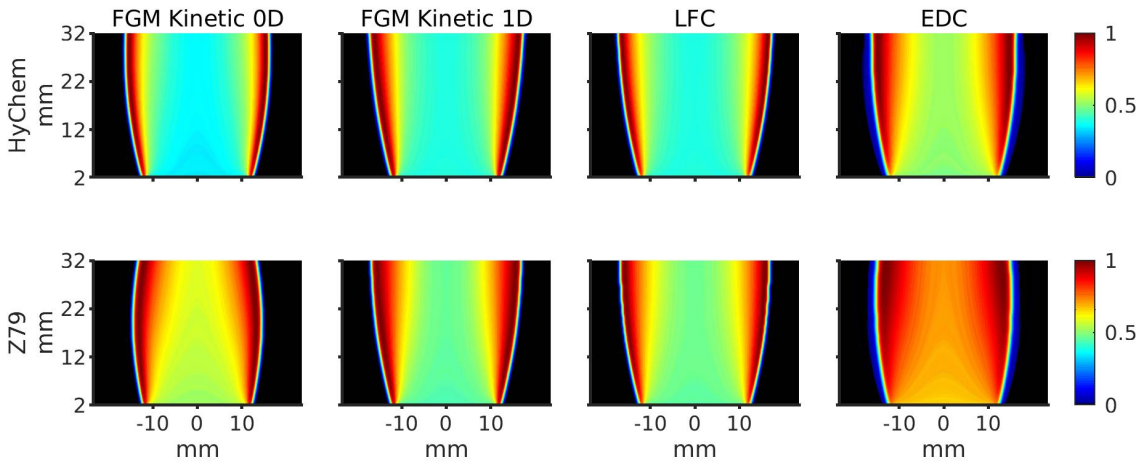

Figure 5.1: OH concentration for 2D RANS. Row 1 presents the HyChem reaction mechanism results, and row 2 presents the Z79 results.

From the CH_2O results in Figure 5.2 it can be concluded that Z79 predicts a somewhat thicker CH_2O layer which is consistent with the preheat layer, as discussed in Section 2.1. The result for FGM Kinetic 0D with Z79 is the only one that differs significantly from the rest and is somewhat strange because it seems to have two preheat regions. Usually, the flame front is located after the preheat zone, but in this case, it instead seems that another preheat zone is present after the flame front. The reason for this is unclear but the extent of this strange behavior might be exacerbated by interpolation onto a finer grid when processing the results.

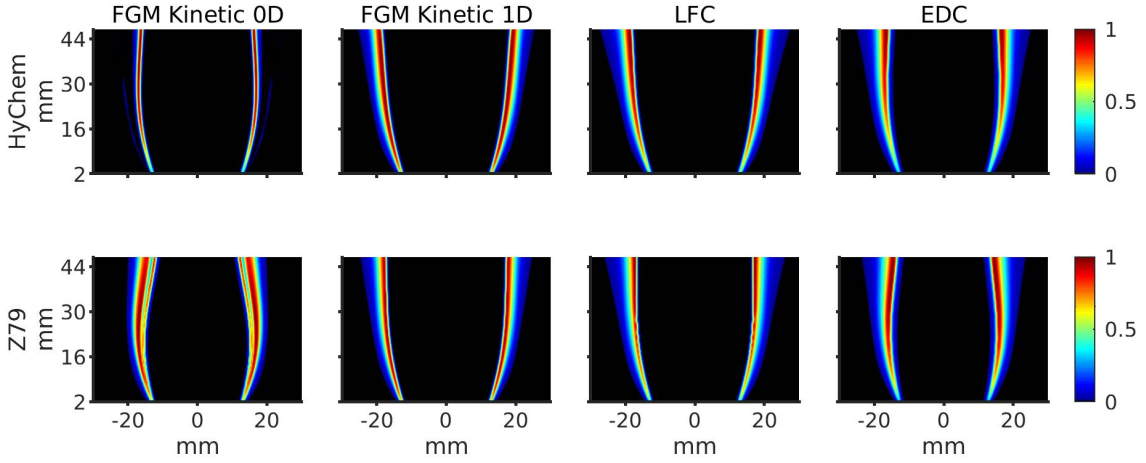

Figure 5.2: CH_2O concentration for 2D RANS. Row 1 presents the HyChem reaction mechanism results, and row 2 presents the Z79 results.

To better quantify the CH_2O results Table 5.1 is given to show the difference in the diameter of the CH_2O region. The diameter was calculated using the maximum value of the CH_2O layer which should be in the center of the preheat layer. The measurement was taken 44 mm downstream of the bluff-body. This positioning was chosen with the expectation that

it would capture data downstream of the widest diameter of the flame, thus indicating that it remains within the recirculation zone. The smallest diameter was predicted by the EDC closely followed by the FGM Kinetic 0D. The largest diameters were predicted by the FGM Kinetic 1D, closely followed by the LFC models. It can also be concluded that Z79 predicted lower diameters for the respective models in comparison to HyChem.

Table 5.1: Diameter $D_{y=44mm}$ of the CH_2O region measured 44 mm downstream from the bluff-body.

Combustion model	**Reaction mechanism**	**D$_{y=44mm}$ [mm]**
FGM Kinetic 0D	HyChem	33.2
FGM Kinetic 1D	HyChem	38.4
LFC	HyChem	37.6
EDC	HyChem	33.6
FGM Kinetic 0D	Z79	30.4
FGM Kinetic 1D	Z79	36.0
LFC	Z79	35.2
EDC	Z79	30.0

Figure 5.3 presents the normalized mean axial velocity $\langle u \rangle / U_b$ for all reacting RANS cases, with axes normalized by bluff-body diameter $D_{bb} = 23$ mm. The results show little to no difference, but it is noteworthy that the FGM Kinetic 1D and LFC models have shorter recirculation zones when compared to the other two models. One explanation for this is that Kinetic 1D and LFC produce strong flames that extend into the bulk flow, thereby reducing the effects made on the recirculation zone. This is supported by the results in Table 5.1, where the diameter of the preheat layer is larger than the recirculation zones, indicating that the flame is not stabilized in the shear layer. Instead, the flame stabilizes independently, no longer relying on the bluff-body for stabilization. Meanwhile, the flames for the Kinetic 0D and EDC models remain within the shear layer and do not extend beyond the recirculation zone in the same manner. Compared to the benchmark, though, all recirculation zones are somewhat short in the axial direction.

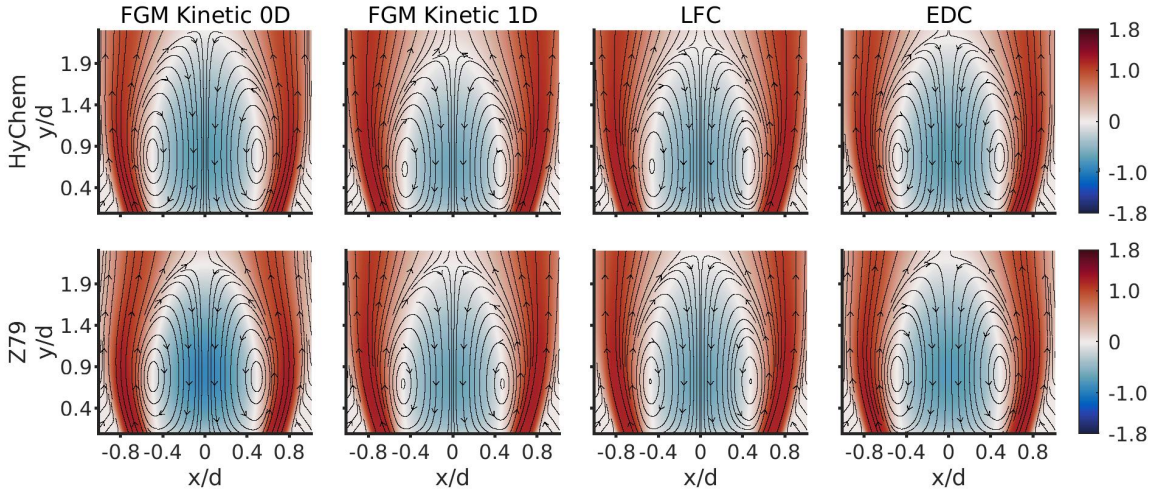

Figure 5.3: Normalized mean axial velocity $\langle u \rangle / U_b$ for all reacting cases.

Following the completion of the study in 2D, a few simulations were conducted in 3D to validate the 2D assumption. The outcomes of these, particularly on an XY-plane, were that they exhibited direct comparability to their corresponding 2D simulations. Consequently, it was determined that employing the 2D approach was satisfactory for analyzing combustion models and reaction mechanisms within the framework of RANS. This result also validated the utilization of the 2D model for mesh and turbulence sensitivity analyses for RANS.

5.2 LES

Table 5.2 presents an overview of the simulation cases that have been performed in LES, including the computational costs.

Table 5.2: Computational cost of each simulation normalized by core-hours/ms for FGM A2.

Combustion model	Fuel	Cost
FGM	A2	1
EDC	A2	5.6
TFM	A2	5.6
TFM Radiation	A2	6.7
FGM	C1	1.4
EDC	C1	5.8
TFM	C1	6.0

It can be concluded that TFM and EDC, both based on Finite Rate Chemistry, are quite computationally expensive. FGM is demonstrably low in cost, which fulfills its purpose as a flamelet model. The radiation model adds to the simulation cost but since the P1 model is quite inexpensive, the difference is not that significant. Some simulations might have run on shared nodes on the supercomputers, which affects computational performance.

5.2.1 OH Structure

Figure 5.4 presents the normalized number density of OH, which is an intensive quantity used for, in this case, visualizing the OH concentration for the FGM, EDC, and TFM setups of both fuels. The data was processed using MATLAB to produce four columns consisting of three instantaneous images and one time-averaged.

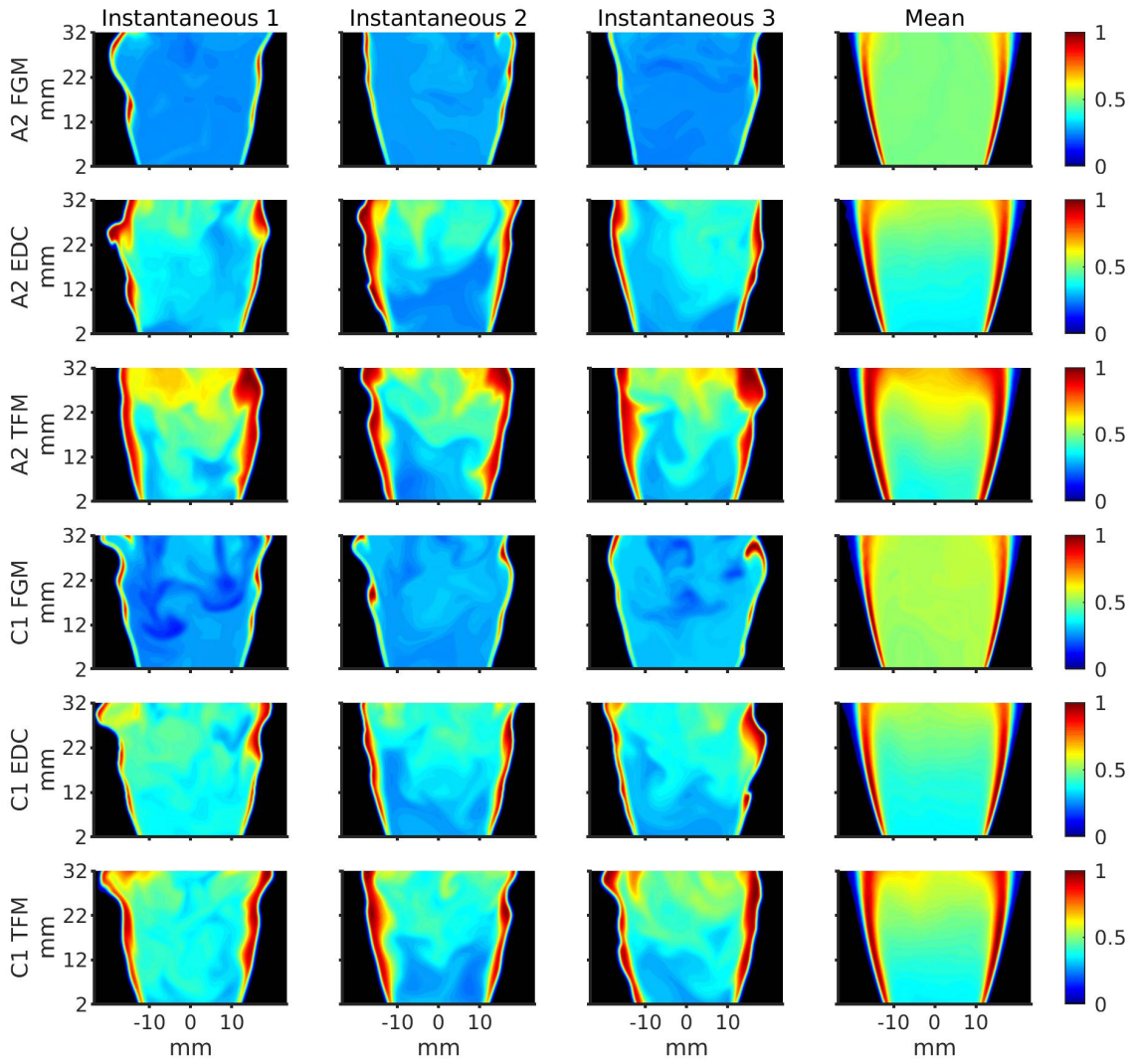

Figure 5.4: Instantaneous and mean OH concentration.

Elevated OH concentrations in the flame front are caused by high OH production during a short time interval which is explained by high reaction rates. This suggests that reactions predominantly occur within a thin region resulting in a strong flame. This is in contrast with the benchmark results that show a high OH-PLIF signal within the whole recirculation zone. The diameter of the flame is also larger in the simulation results which also implies a stronger flame, high reaction rate, and consumption speed.

Focusing on the instantaneous images in Figure 5.4, pockets of high concentration can be seen in the recirculation zone which is congruent with Pathania *et al.* [7]. Both TFM and EDC depict this fairly well while FGM shows this to a lesser extent. The TFM predicts the widest flame front and thus the slowest reaction rate. It is important to note that the benchmark results are obtained from PLIF imaging, whereas the CFD results in this study represent the number density of the radical. Although these are correlated, they are not necessarily proportional. For OH, the differences can be significant because it generally is distributed across a large region.

There is not a significant difference between A2 and C1 in the figure, but it can be concluded

that A2 TFM has a broader flame front than C1, indicated by the larger pockets of high concentration near the edges of the flame.

5.2.2 CH_2O Structure

Figure 5.5 presents the CH_2O concentration results for the FGM, EDC, and TFM setups of both fuels. Same as with OH, these CFD results are number densities rather than PLIF imaging. However, unlike OH, the difference between PLIF imaging and CFD results for CH_2O should not be as significant because the radical is mostly located in the preheat zone, and not as spread out.

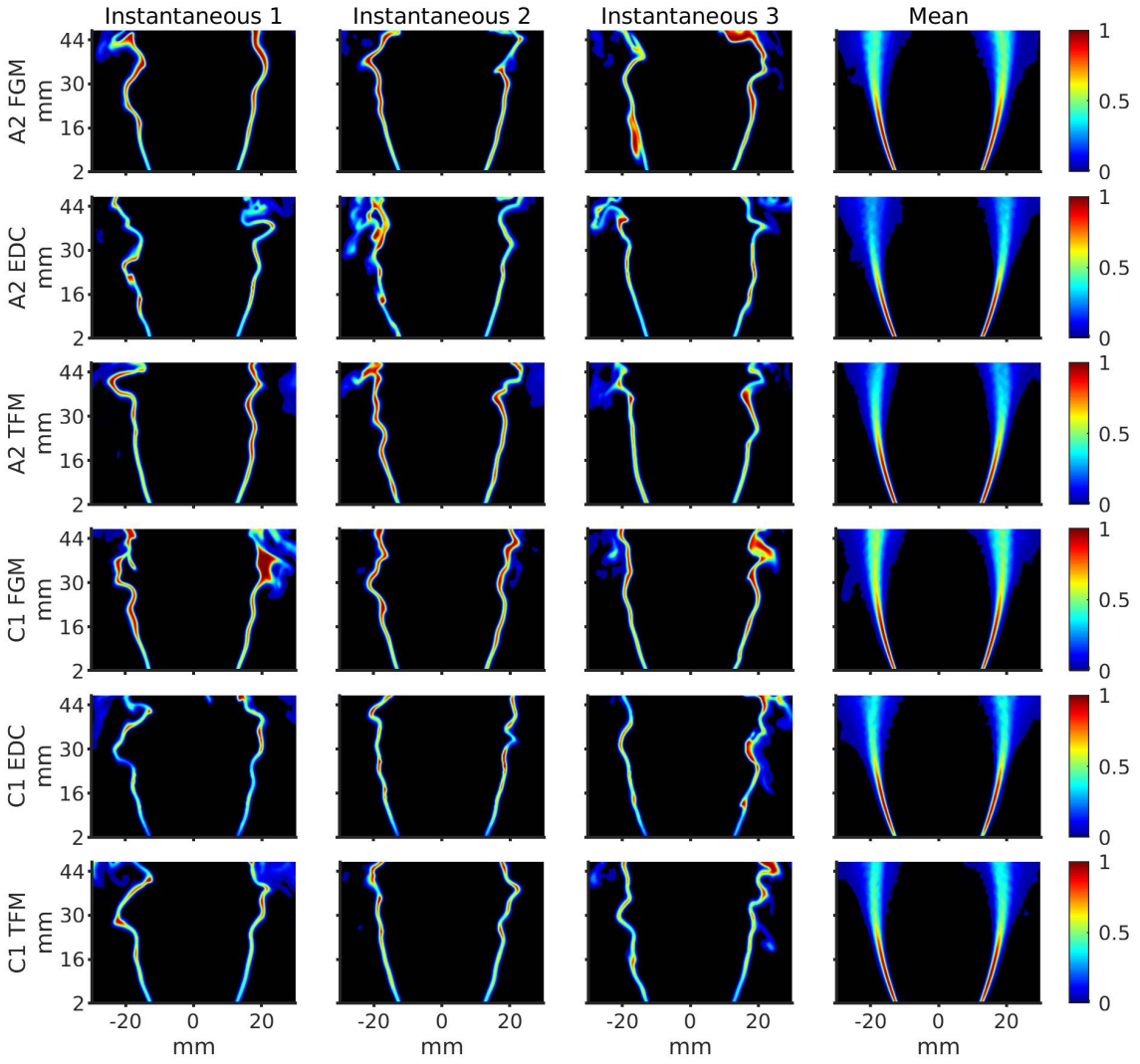

Figure 5.5: Instantaneous and mean CH_2O concentration.

When observing mean CH_2O in Figure 5.5 it can be concluded that the concentration is higher in the anchoring region, close to the bluff-body, for all cases. The red, high-concentration region then transitions into blue/green (lower concentration) downstream, unlike the benchmark result in Figure 4.2 which has a more uniform concentration. A reasonable explanation for this is that the simulations predict thin preheat layers with close to no

broadening. As a result, the concentrations become smoothed out due to a thin yet fluctuating preheat layer when time-averaged.

The simulation results show an asymmetrical flame front wrinkling which is promising as it can be seen in the benchmark results too. However, this asymmetrical wrinkling is significantly weaker compared to the experiments. The Kelvin-Helmholtz instabilities and turbulent eddy effects are not as clear as the small-scale wrinkling remains unresolved, most likely due to mesh resolution. It could also be due to combustion models that overpredict the reaction rate, causing the flame front to resist turbulent fluctuations. Additionally, the boundary conditions of the simulation might not be accurate to the inlet turbulence in the experiments. At an earlier stage of the study, before mass flow scaling was introduced, the wrinkling was symmetrical. This was caused by pressure oscillations, discussed in Section 3.2.

In Table 5.3 it can be seen that the flame with the largest diameter is A2 EDC, with 39.2 mm located 44 mm downstream from the bluff-body, while the smallest is C1 FGM, with 37.0 mm. Generally, it can be concluded that EDC has a larger-diameter flame, which can be caused by a higher reaction rate as discussed in Section 3.4. The high reaction rate observed in the EDC model is a result of the model's improper implementation in LES, causing it to behave similarly to the LFC model, which is known for its high reaction rate.

Table 5.3: Diameter $D_{y=44mm}$ of mean CH_2O region measured 44 mm downstream from the bluff-body.

Combustion model	**Fuel**	**D$_{y=44mm}$ [mm]**
FGM	A2	37.4
EDC	A2	39.2
TFM	A2	37.4
FGM	C1	37.0
EDC	C1	38.0
TFM	C1	37.2

5.2.3 Velocity

Figure 5.6 presents the results for normalized mean axial velocity $\langle u \rangle / U_b$ for all reacting LES cases. The upper row presents the reacting A2 results and the lower row presents the reacting C1 results.

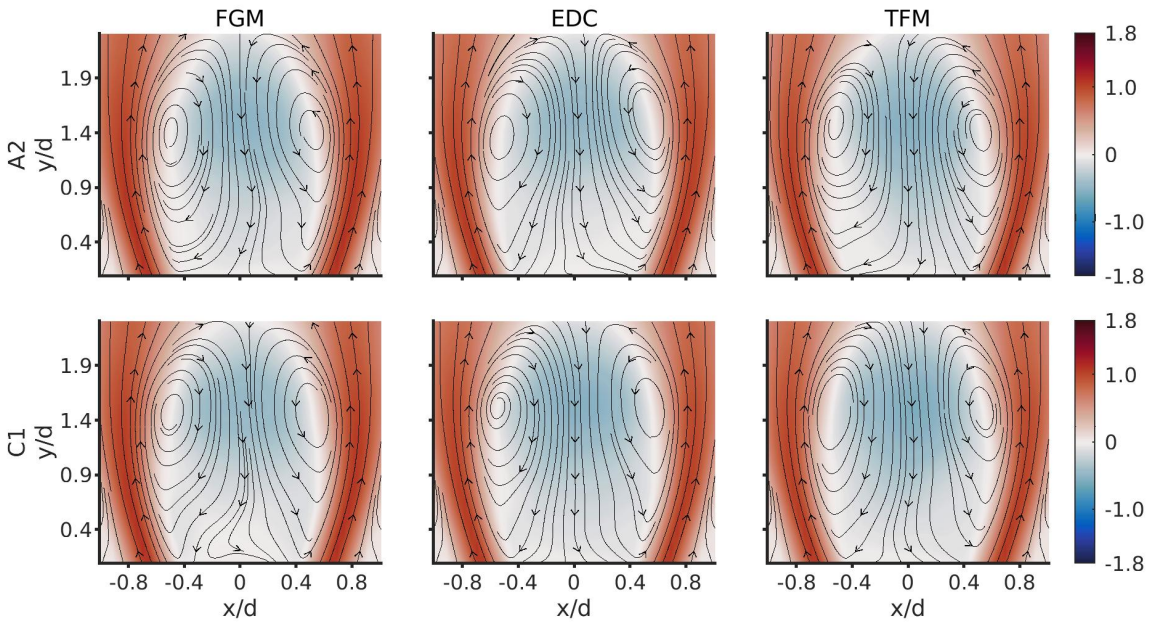

Figure 5.6: Normalized mean axial velocity $\langle u \rangle / U_b$ for all reacting cases.

The results in Figure 5.6 are almost indistinguishable from each other. It can be surmised from the figure, and Table 5.3 that the flame front is situated on the shear layer of the recirculation zone for all LES cases. The length of the recirculation zone is also in better agreement with the benchmark in Figure 4.3 compared to the RANS results.

5.2.4 Turbulence Intensity & Borghi Diagram

Figure 5.7 presents the turbulence intensity (u'/U_b) and integral length scale (L_T) evaluated at six evenly spaced axial locations on the contour where the time-averaged progress variable is $\langle c \rangle = 0.2$, and $\langle c \rangle = 0.5$. The time-averaged progress variable, $\langle c \rangle$, is calculated by averaging the whole dataset of instantaneous OH data after binarizing it with a threshold of either 0.2 or 0.5.

The fluctuating velocity, u', is calculated by first calculating the variance of the velocity snapshots and then taking the square root of the velocity variance. The integral length scale, L_T, is more complex to determine. It involves using the fluctuating velocity results to compute the two-point correlation when moving away from a given location in eight evenly spaced directions. The distance until the two-point correlation reaches zero is measured. This distance is then averaged across the eight directions and is considered the integral length scale. This value theoretically represents the size of the largest turbulent eddies at that location because, within a turbulent eddy, the two-point correlation remains above zero.

It can be observed in Figure 5.7 that the CFD results generally have lower turbulence intensity, u'/U_b, and higher integral length scale, L_T, compared to the benchmark results. The low u'/U_b can be explained by the insufficient turbulence level at the inlet. This aligns with the absence of flame front wrinkling observed in the radical contours presented in previous sections. This can be due to the turbulence sensitivity study conducted in RANS, whose results were directly transferred to LES which if it was done in LES as well probably would

yield a different result.

The results for L_T are significantly high for the anchoring region, close to the bluff-body. The method for calculating the integral length scale assumes the presence of distinct small turbulent eddies in the flame front. If such turbulence is not present to the expected degree, the resulting integral length scale is not accurately defined, something that might cause the high L_T for the three initial measure points. The length scales at the three latter measure points seem to be more in correlation with the experimental results, something that can be explained by more flame wrinkling seen further downstream indicating the presence of turbulent eddies.

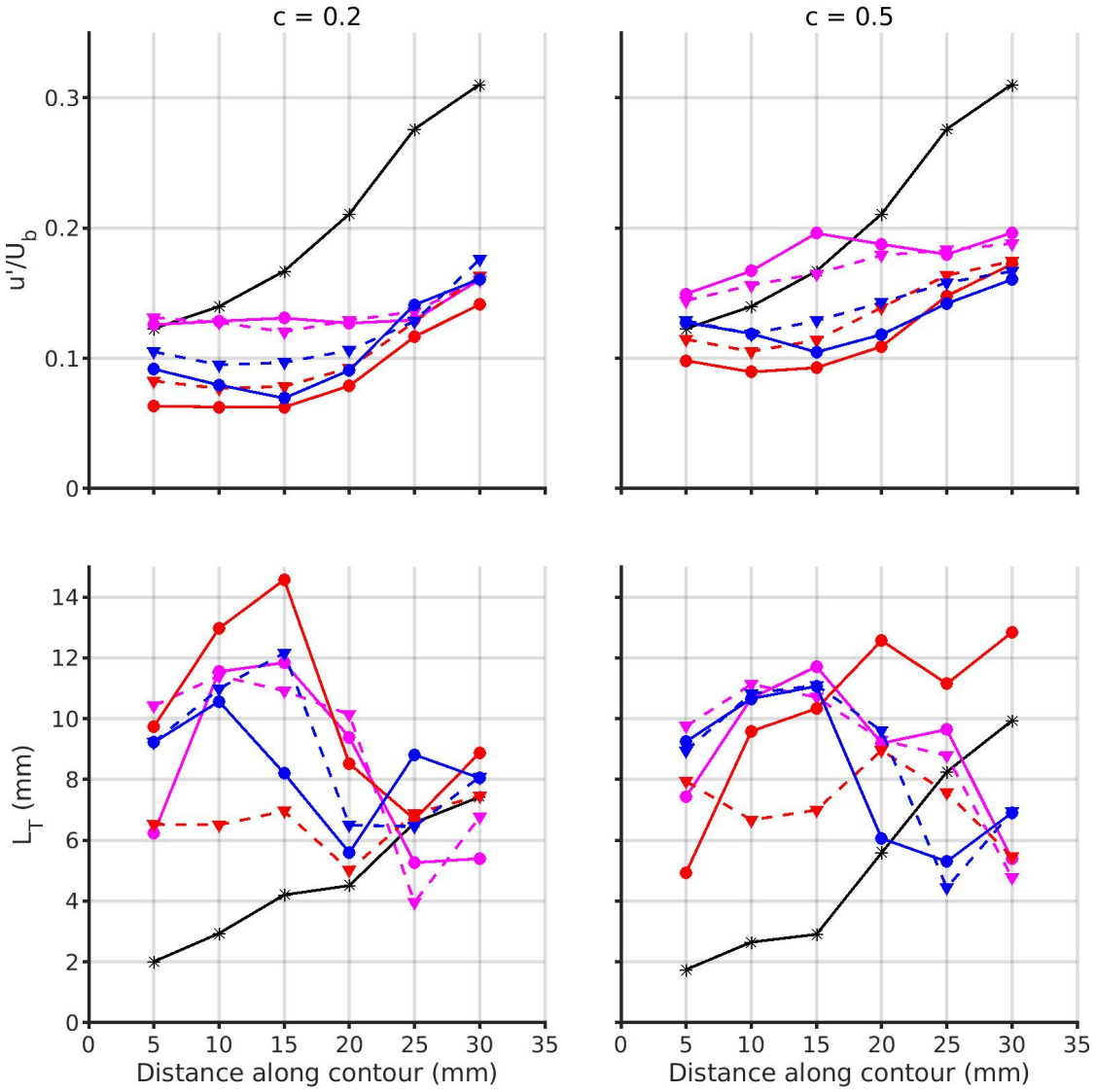

Figure 5.7: Turbulence intensity (u'/U_b) and integral length scale (L_T) evaluated over the contour $c = 0.2$ and $c = 0.5$ in the flame. Red for FGM, blue for EDC, magenta for TFM, and black for experiments [7]. Circles represent A2, and triangles with dashed lines represent C1.

The turbulence intensity and integral length scale can be used to put the data points inside a Borghi diagram. Figure 5.8 presents the Borghi diagram suggested by Skiba *et al.* [41],

which is a modified version of the traditional diagram.

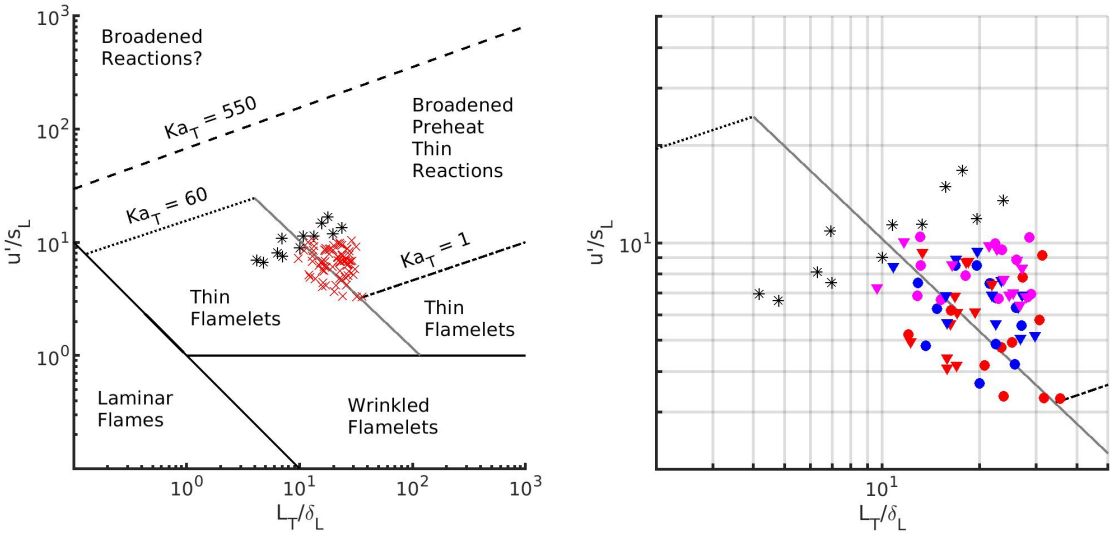

Figure 5.8: Borghi diagram suggested by Skiba *et al.* [41]. Left figure: red '$\times$' for simulations, black '$*$' for experiments [7]. Right figure: zoomed-in Borghi diagram with red for FGM, blue for EDC, magenta for TFM, and black for experiments [7]. Circles and triangles represent A2 and C1, respectively.

All simulation results in Figure 5.8 are spread across two regions—*Thin Flamelets* (T-F) and *Broadened Preheat Thin Reactions* (BP-TR)—just as the benchmark results. T-F denotes flames that have thin preheat and reaction zones, while BP-TR represents flames with broadened preheat and thin reaction zones [41]. The right figure presents the same data, but zoomed-in and more in-depth, clarifying each model and fuel used in comparison to the benchmark results. The TFM results for both fuels (magenta) are almost exclusively in the BP-TR region, and the EDC C1 results (blue triangles) predominantly fall in this region as well. Examining OH and CH_2O in Figures 5.4 and 5.5, it can be concluded that the reaction zone is relatively wide, while the preheat zone remains as thin as in the other models. This is not in correlation with the region denotations given by Skiba *et al.* [41]. This is because the Borghi diagram is not made for incessant analyzing of small differences in data points. Instead, it is used to do more general size comparisons of the magnitudes of the two variables. All the data points are within a tight region and some conclusions can be made. They are somewhat lower in fluctuating velocity than the experiments, but other than that they seem to fit well with experimental results and within the two regions previously mentioned.

5.2.5 NO_x Formation

Figure 5.9 presents the mean NO_x mass fraction results for the FGM, EDC, and TFM setups of both fuels. These results are unnormalized for better comparability.

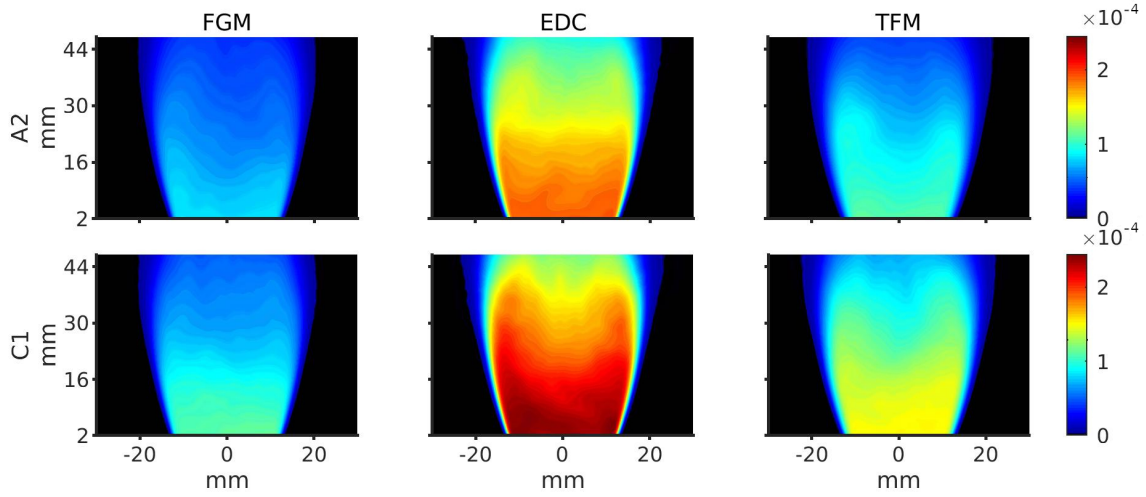

Figure 5.9: Mean NO_x mass fraction in the flame region.

NO_x formation seems to be significantly higher when using the EDC model, for both fuels. It can be concluded that C1 forms more NO_x than A2, throughout all three models. This is to be expected as it has a higher equivalence ratio of 0.85 compared to A2's 0.82. By observing Table 5.4, displaying the maximum temperature for each combustion model's time-averaged temperature plot, it can be concluded that the flame temperature affects the NO_x formation. Specifically, a higher temperature in the flame leads to more NO_x formation, which is consistent with the theory presented in Section 2.9. Further investigation of the relationship leads to the conclusion that combustion models have a greater impact on NO_x formation than temperature differences.

Table 5.4: Max mean temperature in flame.

Combustion model	Fuel	Temperature [K]
FGM	A2	2090
EDC	A2	2090
TFM	A2	2040
TFM Radiation	A2	1910
FGM	C1	2120
EDC	C1	2120
TFM	C1	2070

5.2.6 Thermal Radiation Effects

Figure 5.10 presents comparable results between two A2 TFM simulations, with and without radiation. The quantities that are included in the comparison are OH, CH_2O, NO_x, and temperature.

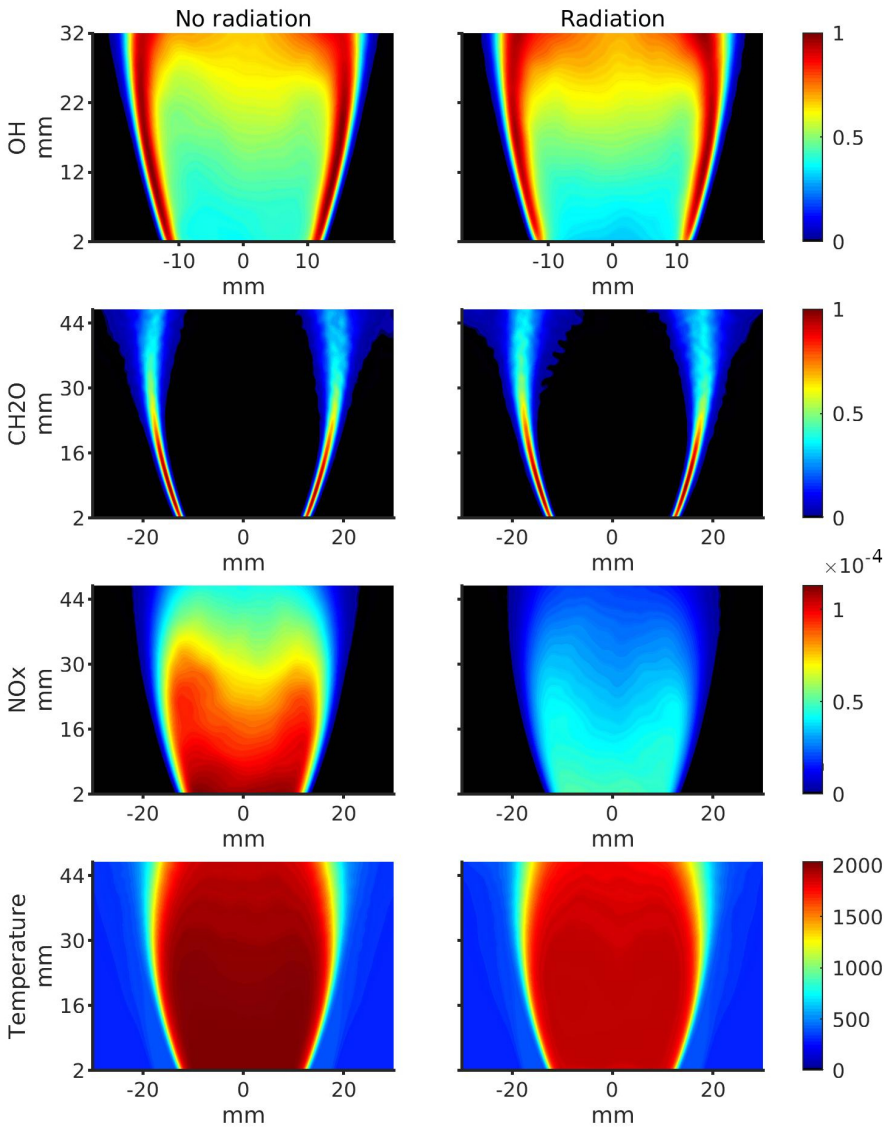

Figure 5.10: Radiation study including OH and CH_2O concentrations, NO_x mass fraction, as well as temperature distribution in kelvin.

It can be seen in Figure 5.10 that OH and CH_2O concentrations are rather similar. With radiation present, the net heat loss causes the flame to drop in temperature and lose energy to the surroundings. This is difficult to observe in the figure, but in Table 5.4 it can be seen that the mean max temperature is 130 K lower when radiation is present. Theoretically, it is unclear how radiation affects the flame since it can both increase and decrease reaction rates, which can either result in a weakened flame or a strengthened flame [40]. By radiating heat, the reactants can absorb heat, enlarging the preheat region and increasing the reaction rate. On the other hand, when the flame radiates heat, it loses energy to the surroundings which leads to a decreased reaction rate according to equation 2.12. As OH and CH_2O seem to be unaffected by radiation, which means that preheat region is unchanged, it could be concluded that the reactants do not absorb radiated heat, due to the way radiation is implemented in STAR-CCM+. The correlated k-distribution [37] is used to model the scattering and absorption effects by calculating the absorption coefficient of gaseous CO_2 and H_2O. This means that the absorption effects of the fuel are left out of the model. They

are most likely negligible because the fuel mass fraction is small, however, it does mean that the preheat zone is unable to absorb radiation using this model since it does not contain the aforementioned species.

6 Conclusion & Future Work

Conclusions following the study are presented here, along with suggestions and improvements for future work.

6.1 Conclusion

- Several combustion models have been tested and validated against the experiments conducted by Pathania *et al.* [7]. The two combustion models that show the best agreement are the Finite Rate Chemistry models EDC and TFM, the former for RANS and the latter for LES. The EDC model shows LFC behavior in LES which indicates that it has not been properly implemented for LES. FGM does give acceptable results in LES for its low computational cost.
- The reaction mechanisms Z79 and HyChem skeletal were compared in the RANS results. Z79 had better agreement with experiments in both the OH distribution and the diameter of the flame. It also has a lower computational cost for FRC models, due to fewer species.
- The NO_x emission results showed that C1 produces more NO_x during combustion, however, since the equivalence ratio is higher than for A2, and consequently the temperature of the flame, this result may be biased, and more investigation is needed to definitively prove this. It can be concluded that the choice of combustion model impacts the results to a higher degree than the temperature in the flame, indicating a high sensitivity to the combustion model when investigating NO_x emissions.
- The thermal radiation effects on the combustion simulation were significant. A reduction of the maximum averaged flame temperature of 130 K was observed and it had a reducing effect on the NO_x production, as expected. Including thermal radiation, even with a simplified model, is computationally expensive, but to neglect the effects of radiation completely is erroneous, especially if the temperature and NO_x emissions are of interest.

6.2 Future Work

Further investigation into this case is necessary, such as the following:

- Conducting a more comprehensive turbulence sensitivity study in LES to ensure the presence of small-scale eddies downstream of the bluff-body.
- Exploring alternative methods to trigger the turbulence in the inlet pipe, such as introducing a grating in the pipe instead of relying solely on synthetic turbulence boundary conditions.

- Investigating the effects of changing the bluff-body angle, as this parameter was not specified in the benchmark [7].
- Examining the NO_x emissions of C1 at the same equivalence ratio as A2 to understand their comparative behavior.
- Exploring additional combustion models available in STAR-CCM+ that were not included in this study.
- Delving deeper into the reaction mechanisms within the HyChem family using LES.

References

[1] GKN Aerospace. *About us*. 2023. URL: https://www.gknaerospace.com/en/about-us/ (visited on 19/12/2023).

[2] M. A. Rumizen. "Qualification of Alternative Jet Fuels". In: *Frontiers in Energy Research* 9 (2021). URL: https://www.frontiersin.org/articles/10.3389/fenrg.2021.760713 (visited on 15/01/2024).

[3] M. Colket, J. Heyne, M. Rumizen, M. Gupta, T. Edwards, W. M. Roquemore, G. Andac, R. Boehm, J. Lovett, R. Williams, J. Condevaux, D. Turner, N. Rizk, J. Tishkoff, C. Li, D. Moder J. Friend and V. Sankaran. "Overview of the National Jet Fuels Combustion Program". In: *AIAA Journal* 55 (2017), pp. 1087–1104. DOI: doi:10.2514/1.J055361.

[4] A. Åkerblom, N. Zettervall and C. Fureby. "Comparing Chemical Reaction Mechanisms for Jet Fuel Combustion in Simulations of a Turbulent Premixed Bluff-Body Burner". In: *Proceedings of the AIAA SciTech 2024 Forum, Orlando, 4-12 Jan.* (2024). DOI: https://doi.org/10.2514/6.2024-0179.

[5] ASTM International. *Standard Specification for Aviation Turbine Fuel Containing Synthesized Hydrocarbons*. 2024. URL: https://www.astm.org/d7566-23b.html (visited on 24/04/2024).

[6] European Council. *RefuelEU aviation initiative: Council adopts new law to decarbonise the aviation sector*. 2023. URL: https://www.consilium.europa.eu/en/press/press-releases/2023/10/09/refueleu-aviation-initiative-council-adopts-new-law-to-decarbonise-the-aviation-sector/ (visited on 27/05/2024).

[7] R. S. Pathania, A. W. Skiba, J. A. M. Sidey-Gibbons and E. Mastorakos. "Experimental Investigation of Unconfined Turbulent Premixed Bluff-Body Stabilized Flames Operated with Vapourised Liquid Fuels". In: *Journal of Propulsion and Power* 37.3 (May 2021), pp. 479–486. DOI: 10.2514/1.B38133. URL: https://arc.aiaa.org/doi/10.2514/1.B38133 (visited on 15/01/2024).

[8] H. Wang, R. Xu, K. Wang, C.T. Bowman, D.F. Davidson, R.K. Hanson, K. Brezinsky and F.N. Egolfopoulos. "A physics-based approach to modeling real-fuel combustion chemistry - I. Evidence from experiments, and thermodynamic, chemical kinetic and statistical considerations". In: *Combustion and Flame* 193 (2018), pp. 502–519.

[9] R. Xu, K. Wang, S. Banerjee, J. Shao, T. Parise, Y. Zhu, S. Wang, A. Movaghar, D.J. Lee, R. Zhao, X. Han, Y. Gao, T. Lu, K. Brezinsky, F.N. Egolfopoulos, D.F. Davidson, R.K. Hanson, C.T. Bowman and H. Wang. "A physics-based approach to modeling real-fuel combustion chemistry - II. Reaction kinetic models of jet and rocket fuels". In: *Combustion and Flame* 193 (2018), pp. 520–537.

[10] K. Wang, R. Xu, T. Parsie, J. Shao, A. Movaghar, D.J. Lee, J. Park, Y. Gao, T. Lu, Egolfopoulos F.N., D.F. Davidson, R.K. Hanson, C.T. Bowman and H. Wang. "A physics-based approach to modeling real-fuel combustion chemistry - IV. HyChem Modeling of Combustion Kinetics of a Bio-derived Jet Fuel and Its Blends with a Conventional Jet A". In: *Combustion and Flame* 198 (2018), 477–489.

[11] N. Zettervall. "Methodology for developing reduced reaction mechanisms, and their use in combustion simulations". Ph.D. dissertation. Department of Physics, Lund University, Lund, 2021.

[12] T. Poinsot and D. Veynante. *Theoretical and Numerical Combustion*. R.T. Edwards, Inc., 2001, pp. 66–70, 125.

[13] S. Friedlander and D. Serre. "Localized Instabilities in Fluids". In: *Handbook of Mathematical Fluid Dynamics* (2003). DOI: https://doi.org/10.1016/S1874-5792(03)80010-1.

[14] H.K. Versteeg and W. Malalasekera. *An Introduction to Computational Fluid Dynamics*. Pearson Education Limited, 2007.

[15] E. Fedina. "Post-Detonation Afterburning of High Explosives". PhD thesis. Department of Energy Sciences, Lund University, Lund, 2017.

[16] W. Sutherland. "LII. The Viscosity of Gases and Molecular Force". In: *The London, Edinburgh, and Dublin Philosophical Magazine and Journal of Science* 36.223 (1893), pp. 507–531. DOI: https://doi.org/10.1080/14786449308620508.

[17] R. Courant, H. Lewy and K O. Friedrichs. *On the partial difference equations of mathematical physics*. New York: Courant Institute of Mathematical Sciences, New York University, 1956.

[18] C. T. Chong and J-H. Ng. "Chapter 4 - Combustion Performance of Biojet Fuels". In: *Biojet Fuel in Aviation Applications* (2021), pp. 175–230. DOI: https://doi.org/10.1016/B978-0-12-822854-8.00002-0.

[19] E. Fedina, C. Fureby, G. Bulat and W. Meier. "Assessment of Finite Rate Chemistry Large Eddy Simulation Combustion Models". In: *Flow, Turbulence and Combustion* 99 (2017), pp. 385–409. DOI: https://doi.org/10.1007/s10494-017-9823-0.

[20] S. B. Pope. *Turbulent Flows*. Cambridge University Press, 2000.

[21] F. Nicoud and F. Ducros. "Subgrid-Scale Stress Modelling Based on the Square of the Velocity Gradient Tensor". In: *Flow, Turbulence and Combustion* 62 (Sept. 1999), pp. 183–200. DOI: https://doi.org/10.1023/A:1009995426001.

[22] B. F Magnussen. "THE EDDY DISSIPATION CONCEPT A BRIDGE BETWEEN SCIENCE AND TECHNOLOGY". In: *ECCOMAS Thematic Conference on Computational Combustion, Lisbon, 21-24 Jun.* (2005).

[23] A. Åkerblom. "Turbulence-chemistry interaction in OpenFOAM and how to implement a dynamic PaSR model for LES of turbulent combustion". In: *Proceedings of CFD with OpenSource Software* (2022). DOI: http://dx.doi.org/10.17196/OSCFD#YEAR2022.

[24] M. Bösenhofer, E-M. Wartha, C. Jordan and M. Harasek. "The Eddy Dissipation Concept—Analysis of Different Fine Structure Treatments for Classical Combustion". In: *Energies* 11 (2018). DOI: https://doi.org/10.3390/en11071902.

[25] B. Panjwani, I. S. Ertesvåg, K. E. Rian and A. Gruber. "Subgrid Combustion Modeling for Large Eddy Simulation (LES) of Turbulent Combustion Using Eddy Dissipation Concept". In: *ECCOMAS CFD, Lisbon, 14-17 Jun.* (2010).

[26] L. Durand and W Polifke. "Implementation of the Thickened Flame Model for Large Eddy Simulation of Turbulent Premixed Combustion in a Commercial Solver". In: *Proceedings of the ASME Turbo Expo 2007: Power for Land, Sea, and Air, Montreal, 14-17 May* 2 (2007), pp. 869–878. DOI: 10.1115/GT2007-28188.

[27] J. C. Massey, I. Langella and N. Swaminathan. "Large Eddy Simulation of a Bluff Body Stabilised Premixed Flame Using Flamelets". In: *Flow, Turbulence and Combustion* 101 (2018), pp. 973–992. DOI: https://doi.org/10.1007/s10494-018-9948-9.

[28] H. Lehtiniemi, F. Mauß, M. Balthasar and I. Magnusson. "Modeling diesel spray ignition using detailed chemistry with a progress variable approach". In: *Combustion Science and Technology* 178 (2006), pp. 1977–1997. DOI: https://doi.org/10.1080/00102200600793148.

[29] V. Zimont, W. Polifke, M. Bettelini and W. Weisenstein. "An Efficient Computational Model for Premixed Turbulent Combustion at High Reynolds Numbers Based on a Turbulent Flame Speed Closure". In: *Journal of Engineering for Gas Turbines and Power* 120 (1998). DOI: 10.1115/1.2818178.

[30] A. Scholtissek, P. Domingo, L. Vervisch and C. Hasse. "A self-contained progress variable space solution method for thermochemical variables and flame speed in freely-propagating premixed flamelets". In: *Proceedings of the Combustion Institute* 37 (2018). DOI: 10.1016/j.proci.2018.06.168.

[31] J. Edwards. "Reference Jet Fuels for Combustion Testing". In: *Proceedings of the 55th AIAA Aerospace Sciences Meeting, Grapevine, 9-13 Jan.* (2017). DOI: 10.2514/6.2017-0146.

[32] Peter B.D. de la Mare. *Reaction Mechanism*. 2022. URL: https://www.britannica.com/science/reaction-mechanism (visited on 06/03/2024).

[33] M. Pronobis. *Environmentally Oriented Modernization of Power Boilers*. Elsevier Inc., 2020, pp. 79–128. ISBN: 978-0-12-819921-3.

[34] R. Miller, G. Davis, G. Lavoie, C. Newman and T. Gardner. "A Super-Extended Zel'dovich Mechanism for No x Modeling and Engine Calibration". In: *SAE Transactions* 107 (1998), pp. 1090–1100. URL: https://www.jstor.org/stable/44736596.

[35] G. G. De Soete. "Overall reaction rates of NO and N2 formation from fuel nitrogen". In: *Symposium (International) on Combustion* 15 (1975), pp. 1093–1102. DOI: https://doi.org/10.1016/S0082-0784(75)80374-2.

[36] M. F Modest. *Radiative Heat Tansfer*. Third Edition. Elsevier, 2013.

[37] M. F. Modest and H. Zhang. "The Full-Spectrum Correlated-k Distribution for Thermal Radiation From Molecular Gas-Particulate Mixtures". In: *Journal of Heat Transfer* 124 (2001), pp. 30–38. DOI: https://doi.org/10.1115/1.1418697.

[38] A. C Eckbreth. *Laser Diagnostics for Combustion Temperature and Species*. Taylor Francis Group, 1996.

[39] V. Venkatakrishnan. “On the Accuracy of Limiters and Convergence to Steady State Solutions”. In: *Proceedings of the 31st AIAA Aerospace Sciences Meeting, Reno, 11-14 Jan.* (1993).

[40] A. Åkerblom. Personal Communication. 2024.

[41] A. W. Skiba, T. M. Wabel, C. D. Carter, S. D. Hammack, J. E Temme and J. F. Driscoll. “Premixed flames subjected to extreme levels of turbulence part I: Flame structure and a new measured regime diagram”. In: *Combustion and Flame* 189 (2018), pp. 407–432. DOI: https://doi.org/10.1016/j.combustflame.2017.08.016.

A Appendix

A.1 Division of Work

Throughout this master's thesis, we have collaborated closely on various aspects of the research, contributing our respective expertise and insights. While the majority of the work was conducted collaboratively, certain tasks were allocated based on individual strengths and interests. Måns took the lead in software areas such as post-processing results using MATLAB. Meanwhile, David concentrated on delving into the theoretical background of the study. The implementation and setup of cases in STAR-CCM+ were collaborative endeavors, as neither of us had prior experience with the software. This joint effort was driven by our mutual interest in CFD and in learning more about the subject.

A.2 Project Timeline

A.2.1 Preliminary Timeline

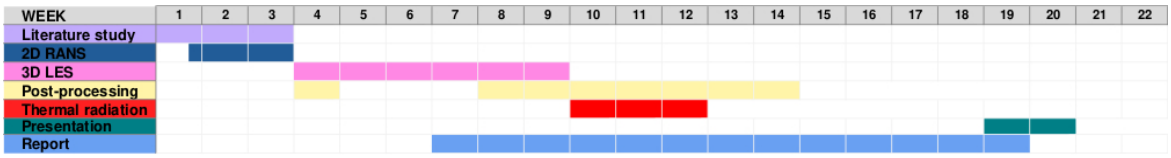

Figure A.1: Preliminary timeline at the initial stage of the project.

A.2.2 Revised Timeline

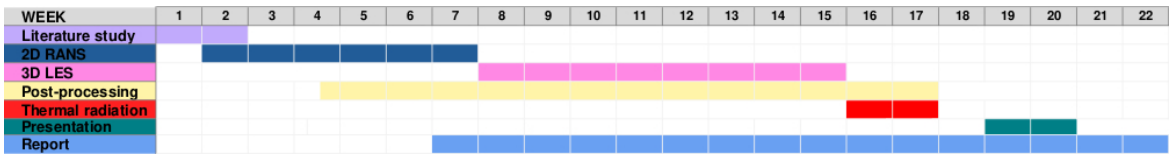

Figure A.2: Revised timeline at the final stage of the project.